Peanut shaped auxetic cementitious cellular composite (ACCC)

Xie, Jinbao; Xu, Yading; Meng, Zhaozheng; Liang, Minfei; Wan, Zhi; Šavija, Branko

DOI
10.1016/j.conbuildmat.2024.135539

Publication date
2024

Document Version
Final published version

Published in
Construction and Building Materials

Citation (APA)
Xie, J., Xu, Y., Meng, Z., Liang, M., Wan, Z., & Šavija, B. (2024). Peanut shaped auxetic cementitious cellular composite (ACCC). *Construction and Building Materials*, *419*, Article 135539. https://doi.org/10.1016/j.conbuildmat.2024.135539

Construction and Building Materials 419 (2024) 135539

Contents lists available at ScienceDirect

Construction and Building Materials

journal homepage: www.elsevier.com/locate/conbuildmat

Peanut shaped auxetic cementitious cellular composite (ACCC)

Jinbao Xie, Yading Xu *, Zhaozheng Meng, Minfei Liang, Zhi Wan, Branko Šavija

Microlab, Faculty of Civil Engineering and Geosciences, Delft University of Technology, Delft 2628CN, the Netherlands

ARTICLE INFO

Keywords:
Auxetic cementitious cellular composites
Additive manufacturing
CDP model
Energy dissipation
Cyclic test
Compressive resilience

ABSTRACT

Auxetic cementitious cellular composites (ACCCs) exhibit desirable mechanical properties (e.g., high fracture resistance and energy dissipation), due to their unique deformation characteristics. In this study, a new type of cementitious auxetic material, referred to as peanut shaped ACCC, has been designed and subsequently architected using additive manufacturing techniques. Two peanut shaped ACCCs specimens with different pseudo-minor axes have been tested under uniaxial compression with Digital Image Correlation (DIC) to assess their compressive behavior, peak strength, Poisson's ratio, and energy dissipation capacity. Additionally, cyclic tests were conducted to investigate their compressive resilience properties, further elucidated through microstructural analysis using a digital optical microscope. The mechanical test results were also compared with those of previously developed elliptical-shaped ACCCs. Furthermore, a numerical model was used to simulate the mechanical behavior of peanut shaped ACCCs under uniaxial compression, and showed a good agreement with the experimental data. The auxetic behavior observed in peanut shaped ACCCs arises from the rotation of sections facilitated by fiber bridging at the ligament of adjacent holes within the cementitious unit cell. In comparison to elliptical-shaped ACCCs, peanut shaped ACCCs can exhibit a slightly more negative Poisson's ratio and mitigate stress concentration. The reduction of stress concentration enables peanut shaped ACCCs to dissipate substantial energy, showcasing enhanced ductility and toughness. In cyclic tests, peanut shaped ACCCs exhibit superior recoverable deformation elasticity, attributed to robust fiber bridging capacity. The exceptional mechanical properties exhibited by peanut shaped ACCCs offer a scalable solution for developing energy-absorbent and multifunctional cementitious materials for smart infrastructure.

1. Introduction

The application of additive manufacturing to cement-based materials opens the potential for developing Architected Cement-based Materials (ACMs). ACMs represent a group of cement-based materials with intricately designed internal geometries at the millimetre to centimetre scale to achieve unique and desired mechanical properties. In general, architected materials are composed of periodic unit cells [1]. The marcoscopic properties of a bulk architected material are determined by the mesoscale geometry of the unit cell and the matrix material. Moini et al. [2] harnessed 3D printing technology to fabricate solidified cement paste elements, crafting bioinspired Bouligand architectures with flaw-tolerant properties and novel performances. Similarly, Sajadi et al. [3] utilized cementitious materials to engineer schwarzite structures by using 3D-printed mold, which effectively enhances the ductility, toughness, and energy absorption potential of cement-based materials. Barri et al. [4] designed multifunctional concrete by introducing a metamaterial paradigm into the creation of concrete for advanced use-case scenarios. This transformative approach empowers construction experts to fine-tune its brittleness, flexibility, and formability while utilizing less of the material without compromising strength or durability. Wan et al. [5] utilized direct ink writing, a 3D printing technology, to fabricate vascular self-healing cementitious materials. This was achieved by purposely incorporating hollow channels within the 3D-printable cementitious matrix.

In traditional construction, cementitious materials are typically cast as solid structures to fully utilize their compressive strength while avoiding their inherent shortcomings under tensile loading. However, the incorporation of short fiber has revolutionized the behavior of cementitious materials, offering remarkable enhancements in tensile performance with a large tensile strain, such as engineered cementitious composite (ECC) [6–11]. This breakthrough has opened new possibilities for casting cementitious materials with intricate geometries, allowing for the creation of structurally diverse and mechanically

* Corresponding author.
E-mail address: y.xu-5@tudelft.nl (Y. Xu).

https://doi.org/10.1016/j.conbuildmat.2024.135539
Received 2 January 2024; Received in revised form 16 February 2024; Accepted 19 February 2024
Available online 23 February 2024

enhanced structures. Ohno et al. [12] created a new framework for simulation and learning-driven design of truss-type ACMs based on ECC, with a focus on high specific energy absorption capability under compression. Inspired by the natural crossed-lamellar structure of conch shells, Zhou et al. [13] utilized "knitting" and "tilting" filaments, two innovative printing patterns, to strengthen the bending performance of a structure. This significantly alleviates anisotropy of 3D printed engineered cementitious composites (3DP-ECC). In our previous study, a so called "indirect" 3D printing technique was used to fabricate a fiber-reinforced cementitious material with elliptical-shaped cellular configurations, known as auxetic concrete or auxetic cementitious cellular composite (ACCC) [14]. This additive manufacturing technique, involving 3D printed negative molds using thermoplastic materials such as acrylonitrile butadiene styrene (ABS), has proven to be an efficient method for producing silicone rubber mold employed in the casting of uniquely shaped cementitious materials.

Materials exhibiting negative Poisson's ratios, categorized as mechanical metamaterials, have increasingly attracted attention recently. Most natural solids exhibit positive Poisson's ratios with expansion in directions perpendicular to the applied compressive force. However, materials with negative Poisson's ratios, also referred to as auxetics, contract in the perpendicular direction under compression and expand laterally when subjected to stretching [15–17]. The distinctive deformation mechanisms of auxetic metamaterials leads to improvements in various mechanical properties, such as high fracture toughness, high damping capability, and high energy absorption. Typically, the auxetic behavior observed in metamaterials is triggered by a local buckling mechanism. Xu et al. [18] employed a fiber-reinforced cementitious composite as the foundational material and crafted a cellular structure featuring periodic elliptical perforations. When subjected to uniaxial compression, the cellular composite demonstrated a distinctive auxetic response characterized by a negative Poisson's ratio. The auxetic behavior in this elliptical-shaped ACCC was attributed to the crack bridging process within the cementitious matrix [14,18]. Following pre-compression to a specific displacement, this elliptical-shaped ACCC, when exposed to cyclic loading, exhibited compliant behavior and a quasi-elastic response. Notably, this exceptional deformation resilience enables the efficient conversion of mechanical energy into alternative forms, such as electricity. This inventive approach has been utilized for energy harvesting by integrating PVDF (Polyvinylidene Fluoride) into the ACCCs [19]. Nevertheless, the elliptical shape of ACCCs introduces significant stress concentration, leading to wider cracks and a reduction in structural ductility. To mitigate stress concentration and enhance crack resistance, further exploration of auxetic behavior achievable through other geometries for cementitious materials is warranted.

Recently, Wang et al. [20] fabricated a peanut-shaped metamaterial by using polylactic acid (PLA). Their test results reveal that the peanut-shaped structure can enhance the negative Poisson's ratio and reduce stress concentration, when compared to the structure with elliptical hole pattern. Similarly, Zhu et al. [21] found that perforated steel structures with peanut shaped holes exhibit exceptional auxetic performance. Likewise, Taherkhani et al. [22] designed a linear piezo-resistive auxetic sensor employing a peanut-shaped auxetic shell made of polydimethylsiloxane (PDMS) rubber. Nonetheless, there have been no attempts of using peanut-shaped auxetic structures manufactured by cementitious materials. The great potential of peanut-shaped cellular configurations in mitigating stress concentration problems and enhancing structural ductility holds paramount importance within the domain of ACCCs. Therefore, the novelty of this paper lies in the fabrication of peanut-shaped ACCCs with a focus on stress concentration mitigation and enhanced crack resistance.

This research has designed and fabricated a novel cementitious auxetic material, termed peanut shaped ACCC, achieved through the integration of peanut shaped voids into the cementitious matrix. The compressive behavior of peanut shaped ACCCs has been analyzed by experiments and numerical models, considering peak strength, Poisson's ratio variation, and energy dissipation capacity. Additionally, effects of varying pseudo-minor axes on the compressive behavior of peanut shaped ACCCs were investigated. Furthermore, a comparison of compressive behaviors between (previously developed) elliptical-shaped ACCCs and peanut shaped ACCCs was conducted. Moreover, cyclic tests were performed to explore their compressive resilience properties, attributed to fiber-bridging mechanisms and structural patterns. These observations were further elucidated through microstructural analysis using a digital optical microscope.

2. Design of peanut shaped ACCCs

The generation of the peanut shaped hole is shown in Fig. 1a (highlighted in red). Firstly, two ellipses, with a half major axis of a and a half minor axis of b, are symmetrically placed around an original point. The ellipses are then offset from the original point by a distance of c. A rectangle in green with a half-height of d is created, and it intersects with the ellipses at four points. Using these four points, two auxiliary circles (represented by dashed lines) are determined with a radius of R and a value of e. Finally, the profile of the peanut shaped hole can be created, as shown in Fig. 1a. As illustrated in Fig. 1b, 1c, a unit cell of the peanut shaped ACCCs is created by subtracting these peanut shaped holes from the square using Boolean operations. The ligament height was defined as l in Fig. 1c. The unit cell was composed of four sections interconnected by four ligaments of adjacent holes, as depicted in Fig. 1. Similar to the major axis and minor axis in elliptical-shaped ACCCs, the pseudo major axis and pseudo minor axis are determined in Fig. 1c for the peanut shaped hole. In general, metamaterials or cellular materials are a distinctive unit cell-based periodic architecture, and their analysis can be conducted using a representative volume element (RVE) with periodic boundary conditions [23–28]. Similarly, ACCCs with multiple cells are periodic cellular materials composed by replicating a single unit cell. As shown in Appendix A, the compression behavior of a representative unit cell in ACCCs can closely mirror that of ACCCs with multiple cells, specifically before reaching the second peak stress of the multiple cells. Hence, the unit cell of the peanut shaped ACCCs was selected for the specimens under investigation.

As indicated in Fig. 1c, the pseudo major axis of the peanut shaped hole is defined as

$$p_a = 4a + 2c \tag{1}$$

In Fig. 1c, the pseudo minor axis of the peanut shaped hole is defined as

$$p_i = 2(d - e) \tag{2}$$

In Fig. 1a, the radius of R of the auxiliary circle can be obtained by

$$R = \frac{\left(a + c - \sqrt{a^2\left(1 - d^2/b^2\right)}\right)^2 + e^2}{2e} \tag{3}$$

In Fig. 1a, the area where two auxiliary circles and the rectangle intersect is as follows:

$$\begin{aligned} A_1 &= 2 * R^2 * \arcsin\left(\frac{a + c - \sqrt{a^2\left(1 - d^2/b^2\right)}}{R}\right) \\ &\quad -2 * \left(a + c - \sqrt{a^2\left(1 - d^2/b^2\right)}\right) * (R - e) \end{aligned} \tag{4}$$

In Fig. 1a, the area where two peanut-shaped holes and the rectangle intersect is as follows:

$$\begin{aligned} A_2 &= ab * \sin\left(2\left(\arccos\left(-\sqrt{1 - d^2/b^2}\right) - \pi\right)\right) \\ &\quad -2ab * \left(\arccos\left(-\sqrt{1 - d^2/b^2}\right) - \pi\right) \end{aligned} \tag{5}$$

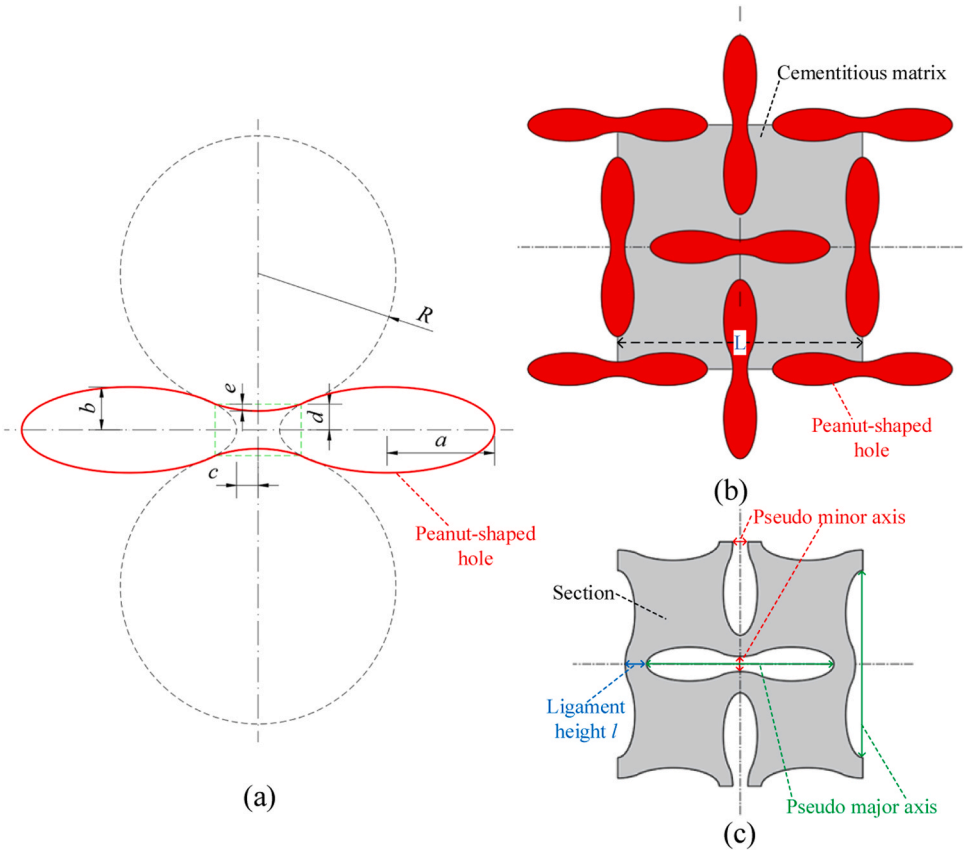

Fig. 1. Generation of the peanut shaped ACCCs, (a) profile of the peanut hole, (b) boolean operations, (c) peanut shaped ACCCs.

Then, the hole area occupied by all peanut-shaped holes within a square (in Fig. 1b) is:

$$A_3 = 2\pi ab + \left(a + c - \sqrt{a^2\left(1 - d^2/b^2\right)}\right) * 4d - A_1 - A_2 \tag{6}$$

The side length of the square (marked in grey in Fig. 1c) is:

$$L = p_a + 2l + p_i \tag{7}$$

Subsequently, the specimen area of the peanut shaped ACCCs in Fig. 1c can be obtained as:

$$A_4 = L^2 - 4A_3 \tag{8}$$

Finally, the relative density of the peanut shaped ACCCs can be defined as:

$$\rho_r = A_4/L^2 \tag{9}$$

Additional details regarding the calculation of Eqs. (1)-(9) can be found in Appendix B.

3. Experiments

3.1. Materials and specimen preparation

The dimensions of ACCCs with three different shapes are illustrated in Fig. 2. In our earlier research [14,18], we observed that the deformed elliptical-shaped ACCCs under compression bears a remarkable resemblance to the geometric shape exhibited by peanut-shaped ACCCs. Therefore, we introduced two distinct peanut shaped ACCCs configurations with different pseudo minor axe, designated as P2 and P3, and conducted a comprehensive analysis, as delineated in Fig. 2. As a reference point for comparative analysis, we also included the elliptical-shaped ACCCs (Fig. 2), referred to as P1. The minor axis/pseudo minor axis of the central hole of ACCC specimens indicates the deformable space, or the compression space under compression. From P3 to P1, the minor axis/pseudo minor axis increases in an approximately twofold relationship. The ligament height l remains consistent at 3.5 mm across all ACCC specimens. Table 1 gives design parameters for different ACCC specimens. Table 1 lists design parameters of these ACCC specimens. Herein, hole area A_3 is calculated by Eq. (6). Specimen area A_4 is calculated by Eq. (8). The relative density ρ_r is calculated by Eq. (9).

The ACCC specimens were fabricated using the so-called "indirect printing" process [18,19] (Fig. 3): (1) Initially, the designed unit cell was created using a Fused Deposition Modeling (FDM) [29] 3D printer, specifically the Ultimaker 2+, with ABS (Acrylonitrile Butadiene Styrene) employed as the printing material. Subsequently, the printed ABS shapes were affixed within a cardboard box. A two-component silicone rubber, specifically Poly-Sil PS 8510, was subsequently mixed in a 1:1 mass ratio and poured into the box. The silicone rubber was cured at room temperature for a minimum of one hour until it hardened. Then, the solidified silicone rubber could be extracted from the box, serving as a silicone rubber mold for casting of the cementitious materials.

The mixture of ACCCs contained CEM I 42.5 N, fly ash, sand with a grain size ranging from 125 to 250 μm, water, polycarboxylate superplasticizer, viscosity modifying agent (VMA), and fiber. Table 2 provides the mixture compositions of ACCCs, which was tailored based on a ACCC mix developed in our previous study [14]. For the ACCCs, a fine-grained fiber reinforced mortar was employed as the constituent material. The Polyvinyl Alcohol (PVA) fiber produced by Changzhou TianYi Engineering Fiber was used as the reinforcement at a volume fraction of 2%. The physical and mechanical properties of the PVA fiber are presented in Table 3. To improve the fiber distribution, a viscosity modifying agent (VMA) in the form of methylcellulose powder from Shanghai Ying Jia Industrial Development Co. Ltd. was utilized. To achieve the desired

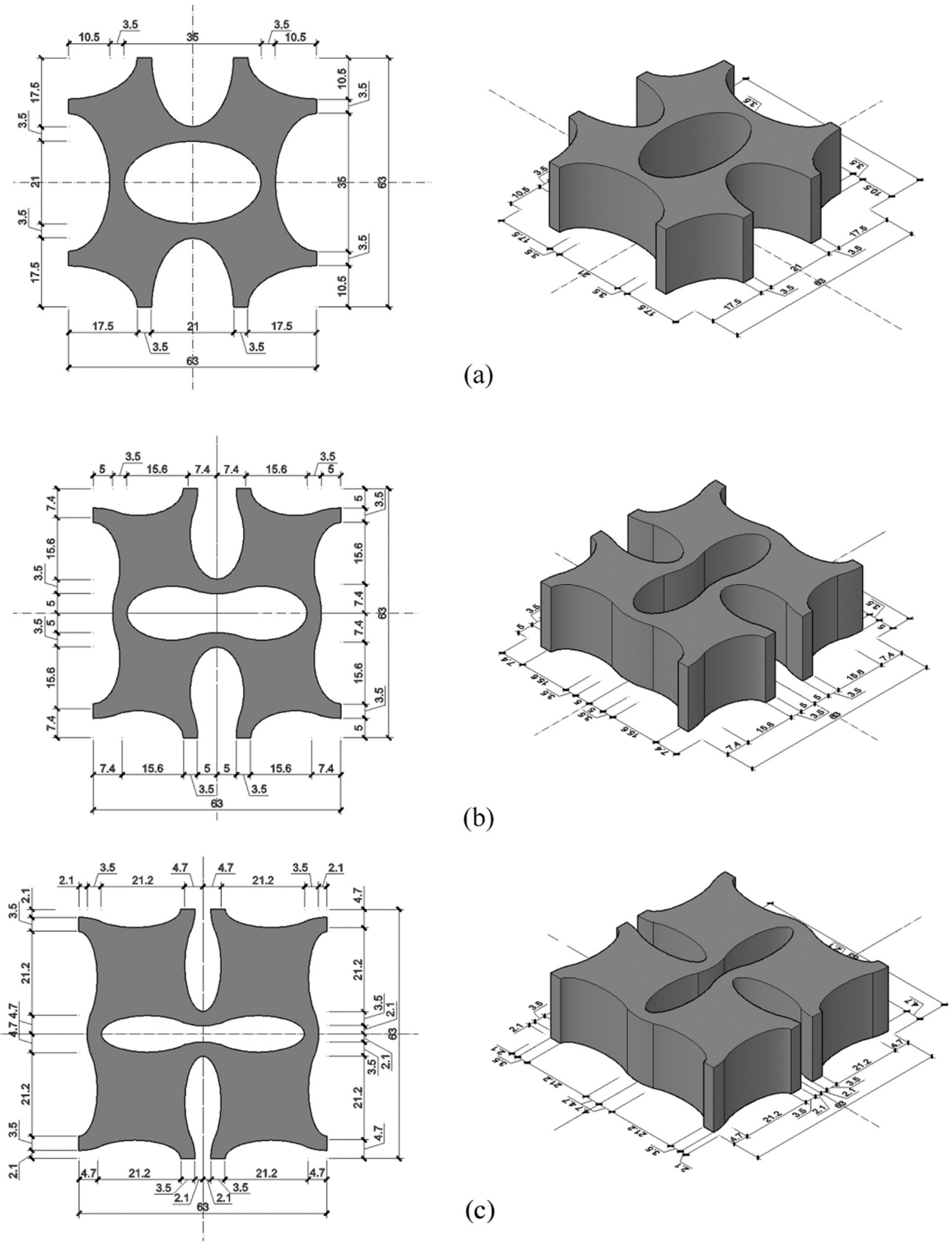

Fig. 2. Dimensions of ACCCs with three different shapes, (a) P1, (b) P2, (c) P3.

Table 1
ACCC specimens with different design parameters.

Specimen	*a* (mm)	*b* (mm)	*c* (mm)	*d* (mm)	*e* (mm)	(Pseudo) major axis (mm)	(Pseudo) minor axis (mm)	Hole area (mm^2)	Specimen area (mm^2)	Relative density
P1	17.5	10.5	-	-	-	35.0	21.0	2309.07	1659.93	41.8%
P2	11.5	6.9	0	6.4	1.4	46.0	10.0	2089.48	1879.52	47.4%
P3	11.8	4.6	2.3	2.8	0.7	51.8	4.2	1463.49	2505.51	63.1%

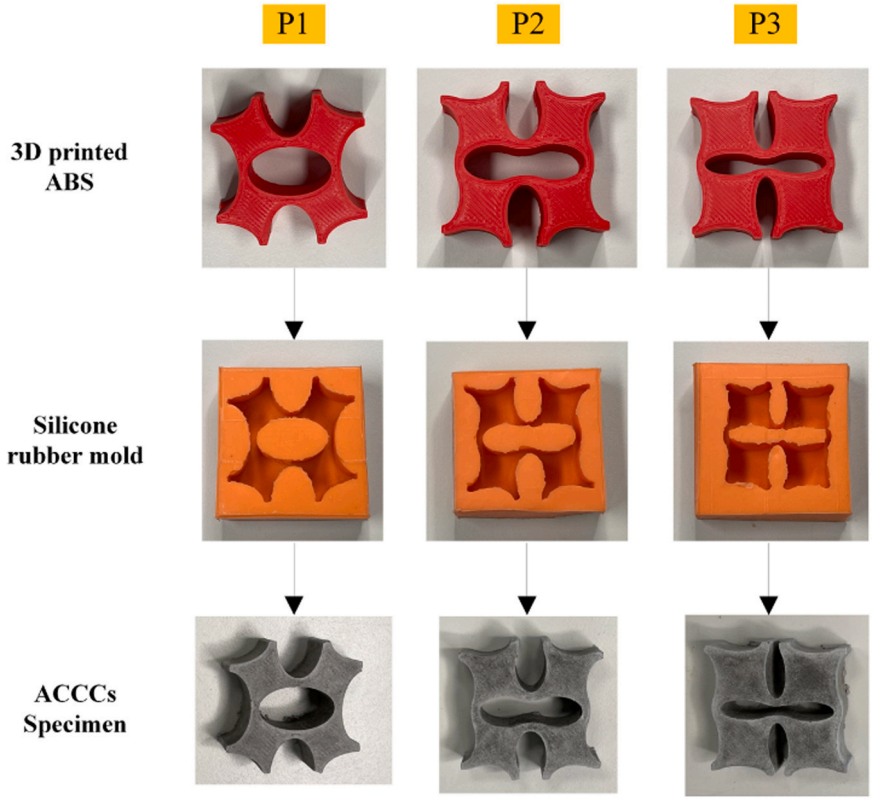

Fig. 3. Procedures of creating ACCCs with three distinct shapes.

Table 2
Mix ratios of ACCCs (kg/m^3).

Cement	Fly ash	Sand (125 μm to 250 μm)	Water	Superplasticizer (Glenium 51)	VMA	PVA Fiber
453	535	370	450	1.58	0.29	25.6

Table 3
Material properties of PVA fiber.

Diameter (μm)	Length (mm)	Tensile strength (MPa)	Young's modulus (GPa)	Density (g/cm3)
15	6	1.6	34	1.28

workability, MasterGlenium 51, a polycarboxylate-based superplasticizer manufactured by BASF (Germany), was utilized. To ensure thorough casting of the cement materials within the small mold, a higher water-to-binder ratio of 0.46 was chosen to facilitate good fluidity.

The dry ingredients including CEM I 42.5, fly ash, sand and VA were mixed for four minutes using a Hobart machine. Water and superplasticizer were then added into the dry mixture, followed by an additional 2 minutes of mixing. Afterwards, the fibers were incorporated into the mortar slowly and mixed for another 2 minutes. To ensure an even distribution of fibers within the matrix, high-speed rotation was further employed to mix the fibers for another 5 minutes. Afterwards, the mixed fresh paste was cast into the silicone molds. Each specimen was filled into the mold in two layers, and each layer underwent 20 seconds of vibration to ensure thorough consolidation. Finally, they were covered with plastic films to prevent evaporation. Following a three-day curing period at room temperature, the specimens were removed from the molds and subsequently placed in a curing chamber (20℃, 96%RH) until the age of 28 days.

3.2. *Experimental test*

In Fig. 4, the uniaxial compression experiments for all ACCC specimens were conducted using a UNITRONIC machine, employing a displacement control method at a rate of 0.01 mm/s. The deformation of the specimens was monitored using Digital Image Correlation (DIC) across their entire area, while the displacement of the specimens was measured by a Linear Variable Differential Transformer (LVDT). DIC is a measurement method that utilizes images captured by cameras to monitor and document the surface movement of a deforming solid. The specimen areas designated for DIC measurements were initially painted in white and then sprayed with a black speckle pattern. During the loading process, images for DIC were consistently captured at 10-second intervals, with a resolution of 0.08 mm/pixel. The DIC results were post-processed using a free version of GOM Correlate software. In each test, the stress-strain curve of ACCC specimens is defined as follows: Stress is

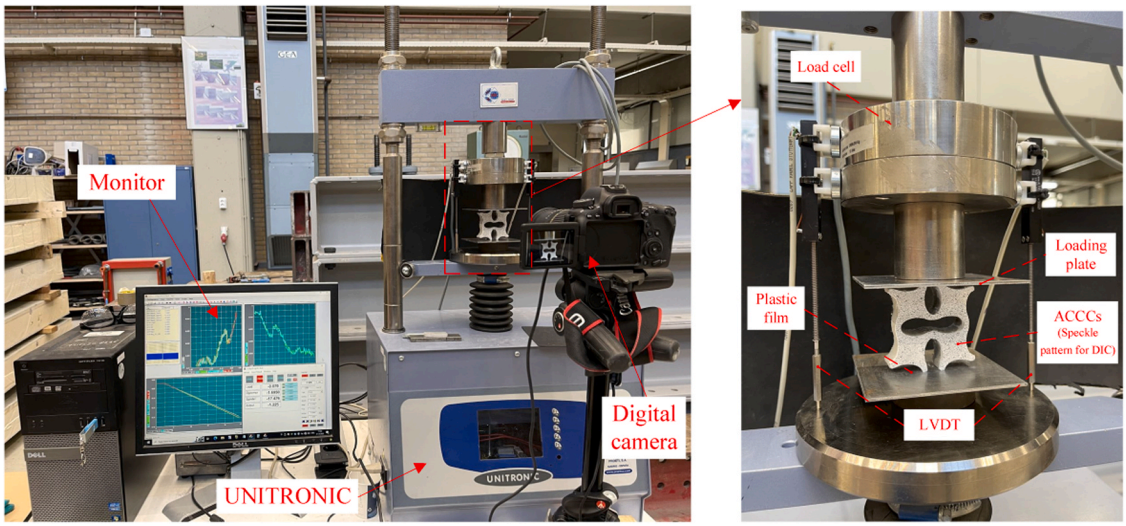

Fig. 4. Experimental setup for the uniaxial compression test.

calculated by dividing the compressive force by the initial cross-sectional area of the specimen, which measures 63 mm×20 mm perpendicular to the loading direction. Strain is determined by dividing the compressive displacement by the initial length of the specimen, which is 63 mm. Plastic films were employed to reduce friction between the ACCCs specimen and the loading plates, facilitating the section rotation necessary for auxetic behavior.

To assess the compressive resilience property of ACCCs, a sinusoidal cyclic test was performed to determine the elastic modulus of compressive resilience. The experimental setup, utilizing the UNITRONIC machine, and the loading plan for the cyclic tests are illustrated in Fig. 5. To accommodate the horizontal movement of ACCCs under cyclic testing, an extended loading plate was selected (Fig. 5a). As depicted in Fig. 5b, the ACCC specimens was initially compressed with a displacement of D_{comp}, followed by a cyclic compression test consisting of multiple cycles of compression and subsequent release. The cyclic testing was conducted at a loading frequency (f) of 0.15 Hz or a loading period (T) of 6.67 seconds, and the loading amplitude (A) was set at 1.0 mm. As indicated in our previous study [19], the pre-compression displacement before cyclic loading D_{comp} was taken as 5.0 mm for elliptical-shaped ACCC specimen P1. Likewise, for peanut shaped ACCC specimens, D_{comp} was selected as 5.0 mm for P2. In the case of specimen P3, a D_{comp} of 4.0 mm was specifically employed to prevent any contact between the upper and lower ends of the peanut-shaped hole. The stress-strain curve in cyclic tests was calculated in the same manner as it is under compression. Three specimens were tested for the same ACCC shape for uniaxial compression and cyclic loading.

4. Numerical modelling

4.1. Model overview

The utilization of the Concrete Damage Plasticity (CDP) model to simulate the elastic–plastic behavior of cementitious composites reinforced by PVA (Polyvinyl alcohol) fibers has been discussed in our earlier publication [14,19]. The constitutive equation of CDP model can be formulated in Eq. (10). Fig. 6 gives the constitutive law of CDP model characterized by tension behavior and compression behavior.

$$\sigma = (1-d)E_0(\varepsilon - \tilde{\varepsilon}^{pl}) \tag{10}$$

where σ refers to the stress; $\varepsilon, \tilde{\varepsilon}^{pl}$ represent the total strain and equivalent plastic strain, respectively. E_0 signifies the initial Young's modulus of the cementitious material. The variable d is utilized as the damage factor, quantifying stiffness degradation within a range of 0–1.0. It requires that the d increases monotonically with strain. However, in the case of utilizing a fiber-reinforced cementitious material, the stress does not follow a monotonic decrease with strain during tension loading. Consequently, stiffness degradation was not considered in this study.

The subscripts t and c in Fig. 6 respectively represent tension and compression. The compressive inelastic strain ε^{in} and tensile crack strain ε^{ck} are determined by subtracting the elastic strain (ε^{el}) corresponding to

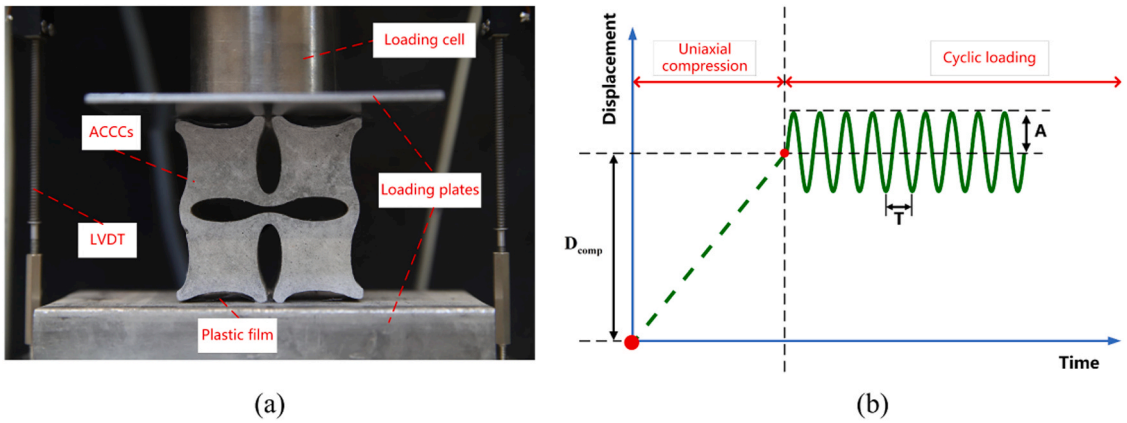

Fig. 5. Cyclic tests of the ACCCs, (a) experimental setup, (b) loading plan.

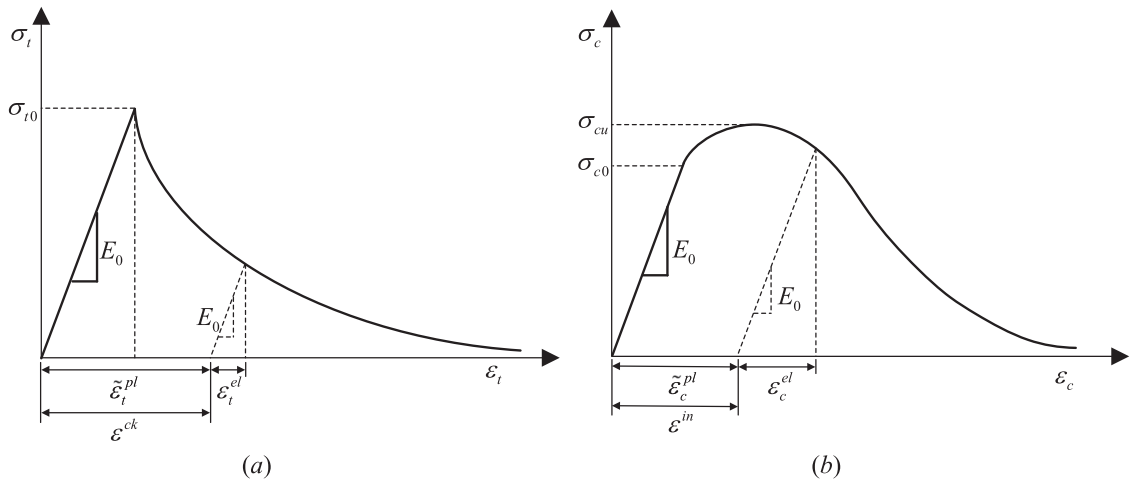

Fig. 6. Constitutive law of CDP model in (a) tension behavior, (b) compression behavior.

the undamaged material from the total strain, respectively. In this study, elastic modulus degradation is not defined; hence, the compressive inelastic strain and tensile cracking strain are assumed to be equal to plastic strain (i.e., $\varepsilon^{in} = \tilde{\varepsilon}_c^{pl}$, $\varepsilon^{ck} = \tilde{\varepsilon}_t^{pl}$), which indicates damage in this model.

The CDP model employs the following yield criterion to characterize the onset of plastic strain.

$$F = \frac{1}{1-\alpha}\left(\bar{q} - 3\alpha\bar{p} + \beta\left(\varepsilon^{pl}\right)\langle\hat{\bar{\sigma}}_{\max}\rangle - \gamma\langle -\hat{\bar{\sigma}}_{\max}\rangle\right) - \hat{\bar{\sigma}}_c\left(\varepsilon_c^{pl}\right) \tag{11}$$

where

$$\alpha = \frac{(\sigma_{b0}/\sigma_{c0}) - 1}{2(\sigma_{b0}/\sigma_{c0}) - 1} \tag{12}$$

$$\beta = \frac{\overline{\sigma_c}\left(\varepsilon_c^{pl}\right)}{\overline{\sigma_t}\left(\varepsilon_t^{pl}\right)} - 1\left(1-\alpha\right) - \left(1+\alpha\right) \tag{13}$$

$$\gamma = \frac{3(1-K_c)}{2K_c - 1} \tag{14}$$

where $\bar{p}$ is the effective hydrostatic pressure. $\bar{q}$ represents the von Mises equivalent effective stress. $\hat{\bar{\sigma}}_{\max}$refers to the maximum principal effective stress. σ_{b0}/σ_{c0} is the ratio of initial equi-biaxial compression yield stress to initial uniaxial compression yield stress. K_c refers to the ratio of the second stress invariant on the tensile meridian to that on the compressive meridian.

Assuming non-associated potential plastic flow within the CDP model, the flow potential G, derived from the Drucker-Prager hyperbolic function, is represented as:

$$G = \sqrt{(\varepsilon_{ec}\sigma_{t0}\tan\psi)^2 + \bar{q}^2} - \bar{p}\tan\psi \tag{15}$$

where ψ is the dilation angle. σ_{t0} is the uniaxial tensile stress at failure. ε_{ec} represents the flow potential eccentricity.

The ABAQUS/explicit module was used for the simulation of the CDP model of ACCCs under quasi-compression. The ACCC specimen was meshed utilizing CPS3, a 3-node linear plane stress triangular element that does not exhibit hourglass effects. The parameters of the CDP model for ACCCs are provided in Table 4. There, ρ is the density of the cementitious matrix. E_0 is the initial Young's modulus of the cementitious matrix. ν is the Poisson's ratio of the cementitious matrix. For the material parameters of CDP model, tensile behavior parameters and compressive behavior parameters for the cementitious matrix were listed in Tables 5and 6, respectively. The loading plates are made of steel with the density of 7800 kg/m^3, the elastic modulus of 206 GPa, and the Poisson's ratio of 0.3. Considering non-linear material behavior and complex interactions, double-precision analysis in the model was utilized to ensure the accuracy of the results.

Table 4
CDP model parameters for ACCC.

ρ_{mix} (kg/m^3)	E_0 (MPa)	ν	σ_{b0}/σ_{c0}	K_c	ψ	ε_{ec}	Viscosity Parameter
1870	3997	0.2	1.16	0.667	35	0.1	0.001

4.2. Model calibration

As depicted in Fig. 7, the tensile behavior of the cementitious matrix was characterized through uniaxial tensile tests. Figs. 7a, 7b depict the configuration of the test setup. These tests were conducted using a TREBEL machine under displacement control, employing a constant loading rate of 0.01 mm/s. The displacement was measured by two linear variable differential transducers (LVDTs) placed on both sides of the specimen. Prior to testing, specimens were glued with a mix of PLEX 7742 F and Pleximon on two parallel (non-rotating) steel plates. Specimen size was 100mmx40mmx10mm after cutting. For each configuration, six bar specimens were used for uniaxial tension tests. The test results in Table 5 can be inputted to the tensile constitutive parameters of the CDP model.

As shown in Fig. 8, the compressive behavior of the cementitious matrix was obtained through uniaxial compression tests. Figs. 8a, 8b illustrate the configuration of the test setup. These tests were conducted using the UNITRONIC machine under deformation control with a displacement rate of 0.01 mm/s. Two LVDTs were attached at each side of the specimen to measure the displacement. A specimen size of 20mmx20mmx20mm was used after cutting. For each configuration, six cubic specimens were used for uniaxial compression tests. The test

Table 5
Tensile behavior parameters.

Yield stress (MPa)	Displacement (mm)
2.358	0
1.283	0.0519
1.671	0.180
1.477	0.265
1.235	0.505
0.959	0.669
0.641	0.962
0.334	1.551
0.193	1.995

Table 6
Compressive behavior parameters.

Yield stress (MPa)	Inelastic strain
8.376	0
12.273	0.0158
12.027	0.0367
10.984	0.0765
10.586	0.0889
10.060	0.1264
9.948	0.1557
10.720	0.2030
11.333	0.2312

results in Table 6 will be inputted as the compressive constitutive parameters of the CDP model for ACCCs.

The parameters of CDP model for the cementitious matrix under tension and compression have been calibrated using experimental data obtained from uniaxial tension and compression tests. Fig. 7c shows a comparison of experimental, model input and calibration curves in uniaxial tension. Fig. 8c also gives a comparison of experimental, model input and calibration curves in uniaxial compression. Both for tension and compression, the simulated results agree well with the experimental data, which indicates that the model is robust, reliable and accurate.

4.3. Simulation of ACCCs under compression

As presented in Fig. 9a, models of three ACCC shapes under uniaxial compression were established. Displacement loading with a small loading rate (i.e., quasi-static loading), was applied to the top plate, while the bottom plate remained fixed (Fig. 9b). Surface-to-surface contact was utilized between ACCCs specimens and loading plate, with their contact surfaces indicated in Fig. 9c. Herein, a low friction coefficient of 0.105 was selected to simulate the slight friction between specimens and the loading plates. To minimize the overclosure (the excessive mutual embedding) between them in the normal direction, a hard contact approach was adopted. During the second phase of compression, the self-contact of ACCC specimen was considered in the model with a sliding friction coefficient of 0.95, a shear stress limit of 0.2 MPa, and an elastic slip stiffness of 2000 MPa. Specifically, a higher shear stress limit of 0.35 MPa was chosen for elliptical-shaped ACCCs. This is attributed to the presence of larger cracks in the ligament of the central hole in elliptical-shaped ACCCs, which elevates the critical shear stress for sliding during the self-contact phase. In the normal direction, a contact stiffness of 3000 MPa was adopted as a linear relationship between contact pressure and overclosure of cementitious material elements. A mesh element size of 0.5 mm was selected following mesh sensitivity analysis.

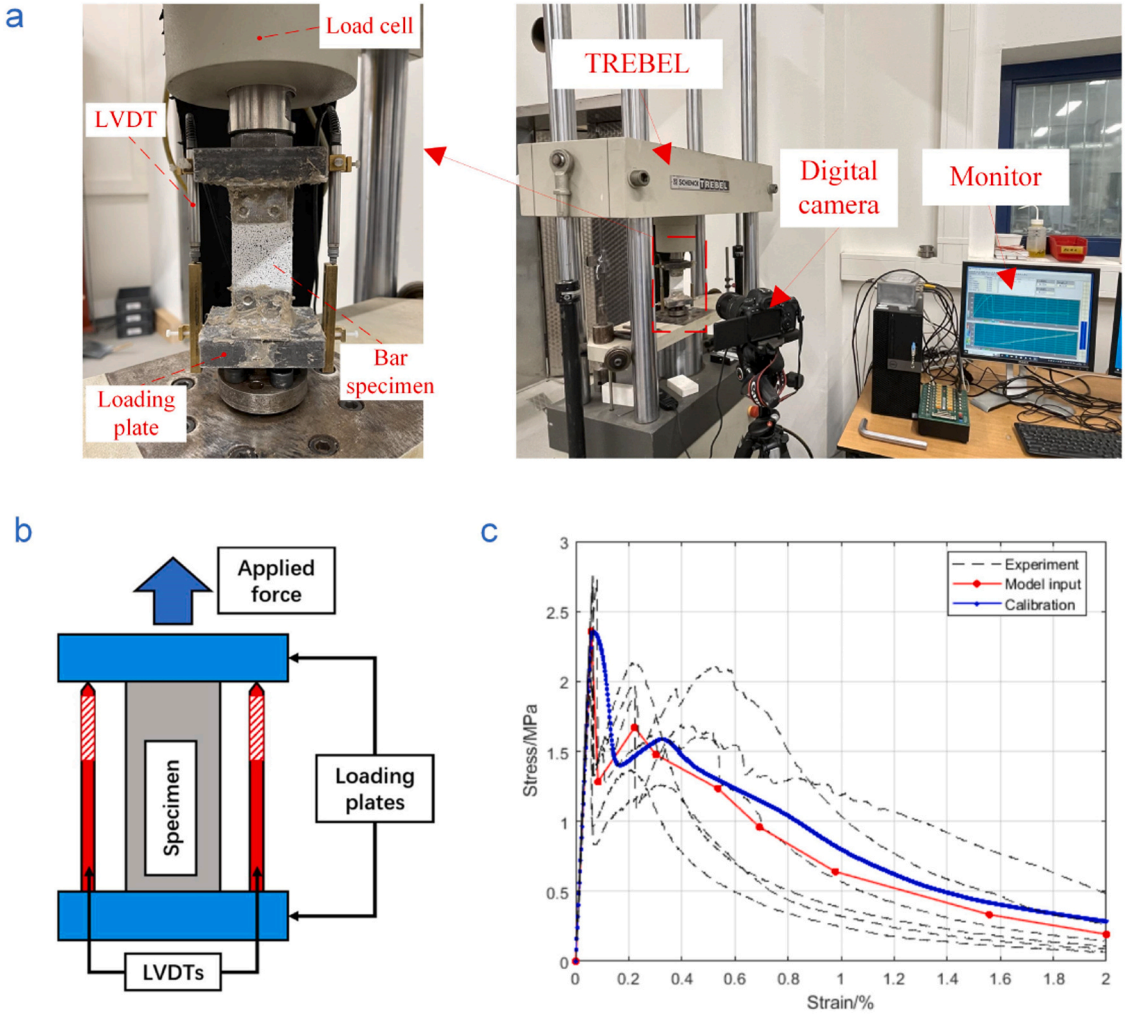

Fig. 7. Comparison of experimental, model input and calibration curves in uniaxial tension.

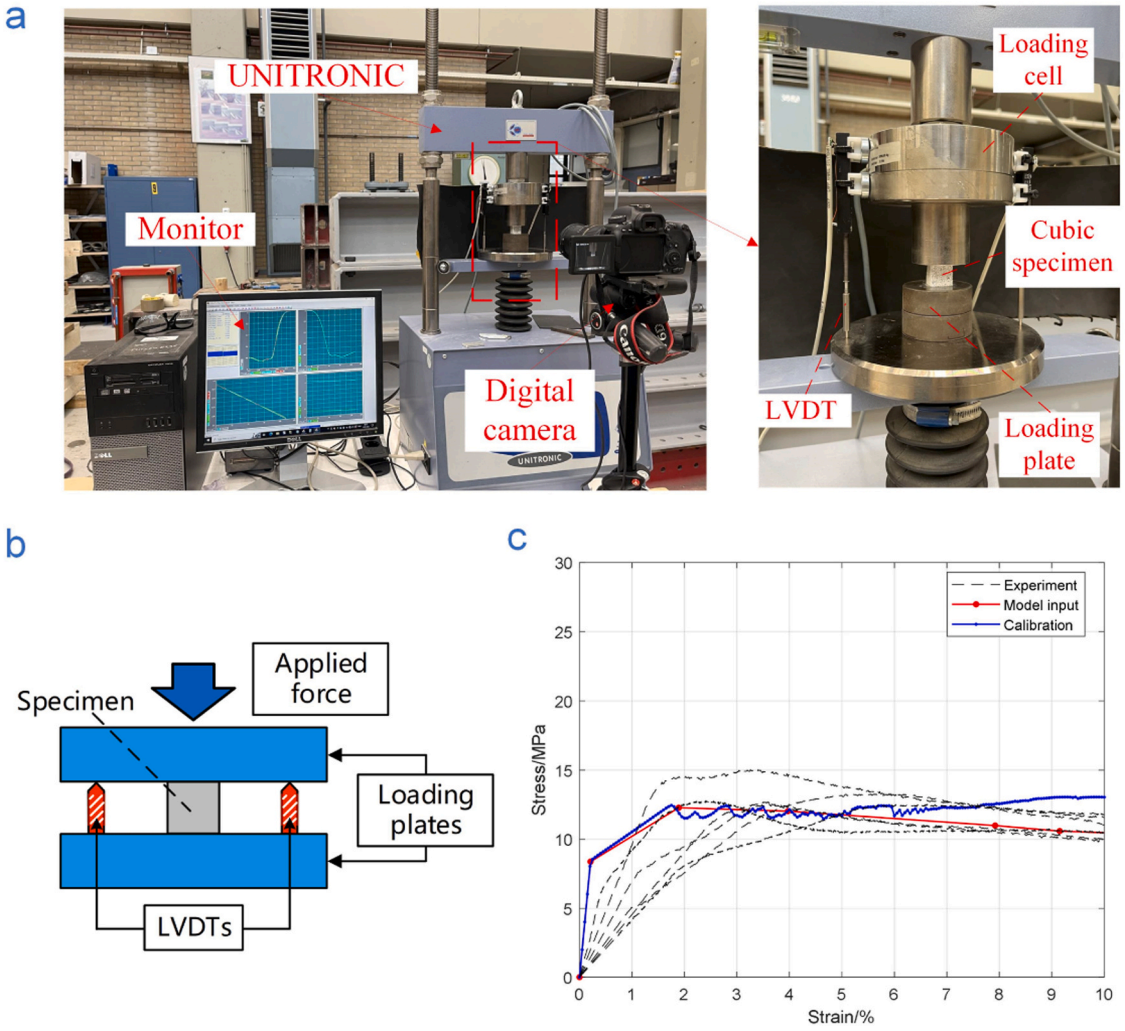

Fig. 8. Comparison of experimental, model input and calibration curves in uniaxial compression.

5. Results and discussion

5.1. Compressive behavior

5.1.1. Compressive stress-strain curve and deformation pattern

Fig. 10, Fig. 11, and Fig. 12 illustrate the uniaxial compression behavior of ACCCs obtained from experimental and numerical results. In Fig. 12, the plastic strain, denoted as 'PE' in the CDP model, serves as a measurable indicator for evaluating crack-induced damage in the ACCC specimens. The mechanical response of elliptical-shaped ACCCs exhibits two discernible stages during uniaxial compression, determined by the cut-off strain when the contact occurs between the top and bottom ends of the central elliptical-shaped hole (i.e., self-contact within the central elliptical-shaped hole). In Stage I, the stress-strain curve of specimen P1 (elliptical-shaped ACCCs) displays an initial increase, reaching the first peak stress at 1.7% strain (averaged across three specimens for each shape in experiments, with the subsequent values obtained in the same manner). Subsequently, it undergoes a decrease until entering Stage II at 19.6% strain when the self-contact occurs within the central elliptical-shaped hole. This is followed by a resurgence, culminating in the second peak stress at 42.2% strain, before declining once more. Similarly, the compression behavior of the peanut-shaped ACCCs also exhibits two stages with two peaks, divided by the cut-off strain associated with the self-contact within the central peanut-shaped hole. In Stage I, specimen P2 shows an initially small increase to reach the first peak stress at 2.95% strain. Afterwards, the stress decreases until it enters Stage II at 12.8% strain, marked by the occurrence of self-contact within the central peanut-shaped hole. In Stage II, the stress continues to increase to the second peak stress at nearly 39.7% strain. In comparison, specimen P3 has the first peak stress at a strain of 2.7% and then drops a little bit. After that, the stress starts to increase at 5.1% strain due to the self-contact within the peanut-shaped hole until it reaches to the second peak stress at 27.9% strain. This strain is lower than specimens P1 and P2, as specimen P3 has the minimum pseudo minor axis and the minimum compression space. In contrast to specimen P1, specimen P2 has a shorter pseudo-minor axis and a smaller compression space, yet its strain at the second peak closely approximates that of specimen P1. This observation indicates that peanut shaped ACCCs exhibit notable improvement in ductility due to the mitigation of stress concentration. Compared to numerical simulations, a slight increase in stress in experimental results was observed just prior to self-contact of the peanut shaped hole. This small stress increase can be attributed to the heterogeneity of cementitious materials, resulting in asymmetric cracking. Consequently, the sections of peanut shaped ACCCs undergo asymmetrical rotation. This rotational behavior is constrained due to their contact with the loading plate, leading to a slight stress increase before the self-contact of central hole. In terms of the uniaxial compressive stress-strain curve and deformation pattern of three ACCCs with different shapes, a good agreement was observed between the experimental data and the numerical results. In the model, the elements with high plastic strain correspond to cracks. However, the edges of these elements with high plastic strain must conform to the self-contact boundary conditions,

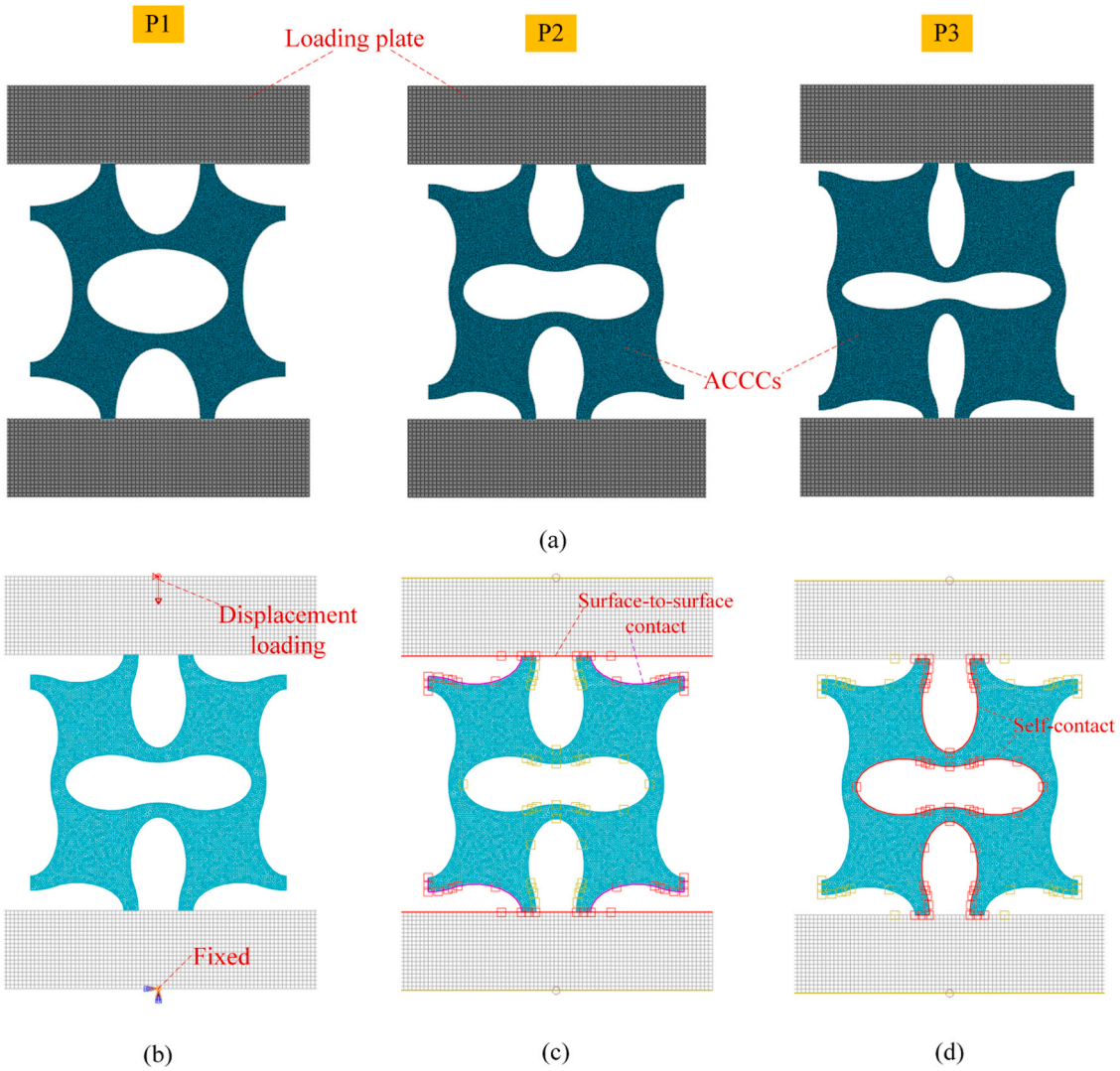

Fig. 9. Modelling of ACCCs under uniaxial compression, (a) finite meshing for ACCCs, (b) boundary conditions, (c) surface-to-surface contact between ACCCs and loading plates, (d) self-contact within ACCCs.

in contrast to the crack, which occupies no physical space. This discrepancy leads to the difference during the self-contact phase between experimental data and numerical results.

Fig. 13 presents a comparative analysis of the first peak stress and the second peak stress among specimens featuring three distinct shapes. Herein, the experiment and simulation results achieve a good agreement in the two peak stresses. Elliptical-shaped specimen P1 exhibits a significantly higher first peak stress of 0.322 MPa in comparison to peanut shaped specimens P2 and P3. Furthermore, it is noteworthy that specimen P2 demonstrates a higher first peak stress of 0.073 MPa compared to the 0.046 MPa observed in specimen P3. Nevertheless, regarding the second stress peak, specimen P3 demonstrates the maximum value of 7.132 MPa in comparison to specimens P1 and P2. Additionally, specimen P1 has a higher second peak stress of 5.335 MPa than the 4.541 MPa of specimen P2.

5.1.2. Poisson's ratio variation

As displayed in Fig. 11 and Fig. 12, the auxetic behavior observed in peanut shaped ACCCs arises from the rotational movement of sections facilitated by fiber bridging at the ligaments of adjacent holes within the cementitious unit cell. Fig. 14 illustrates the variation in Poisson's ratio among ACCC specimens with three distinct shapes in both experimental results and simulations. All specimens exhibit a similar trend: they initially manifest a negative Poisson's ratio in Stage I, undergoing lateral contraction during compression through section rotation induced by limited fiber pull-out. Subsequently, upon self-contact, the absolute value of the negative Poisson's ratio gradually decreases until the specimens undergo lateral expansion under compression, transitioning to a positive Poisson's ratio. In Fig. 14, P3 displays the shortest duration of negative Poisson's ratio, with P2 falling in the middle. In contrast, specimen P1 exhibits the longest duration of negative Poisson's ratio. The duration of the negative Poisson's ratio (i.e., Stage I) is directly proportional to the size of the (pseudo) minor axis of the ACCCs. This relationship arises from the compression space, which facilitates section rotation and contributes to the auxetic behavior. Significantly, P2 and P3 specimens, with different pseudo minor axes in peanut shaped ACCCs, both exhibit their maximum negative Poisson's ratio at around 5% strain. Conversely, P1, the elliptical ACCC specimen, showcases its maximum negative Poisson's ratio at a greater strain of 15%. Regarding the absolute value of negative Poisson's ratio, specimen P3 has the lowest negative Poisson's ratio at 1.05, followed by specimen P1 at 1.12, and specimen P2 exhibits the highest value at 1.25. Despite specimen P2 having a smaller compression space compared to specimen P1, it demonstrates a slightly higher negative Poisson's ratio. This observation suggests that peanut shaped ACCCs have the potential to exhibit a larger negative Poisson's ratio. As displayed in Fig. 14, the model effectively

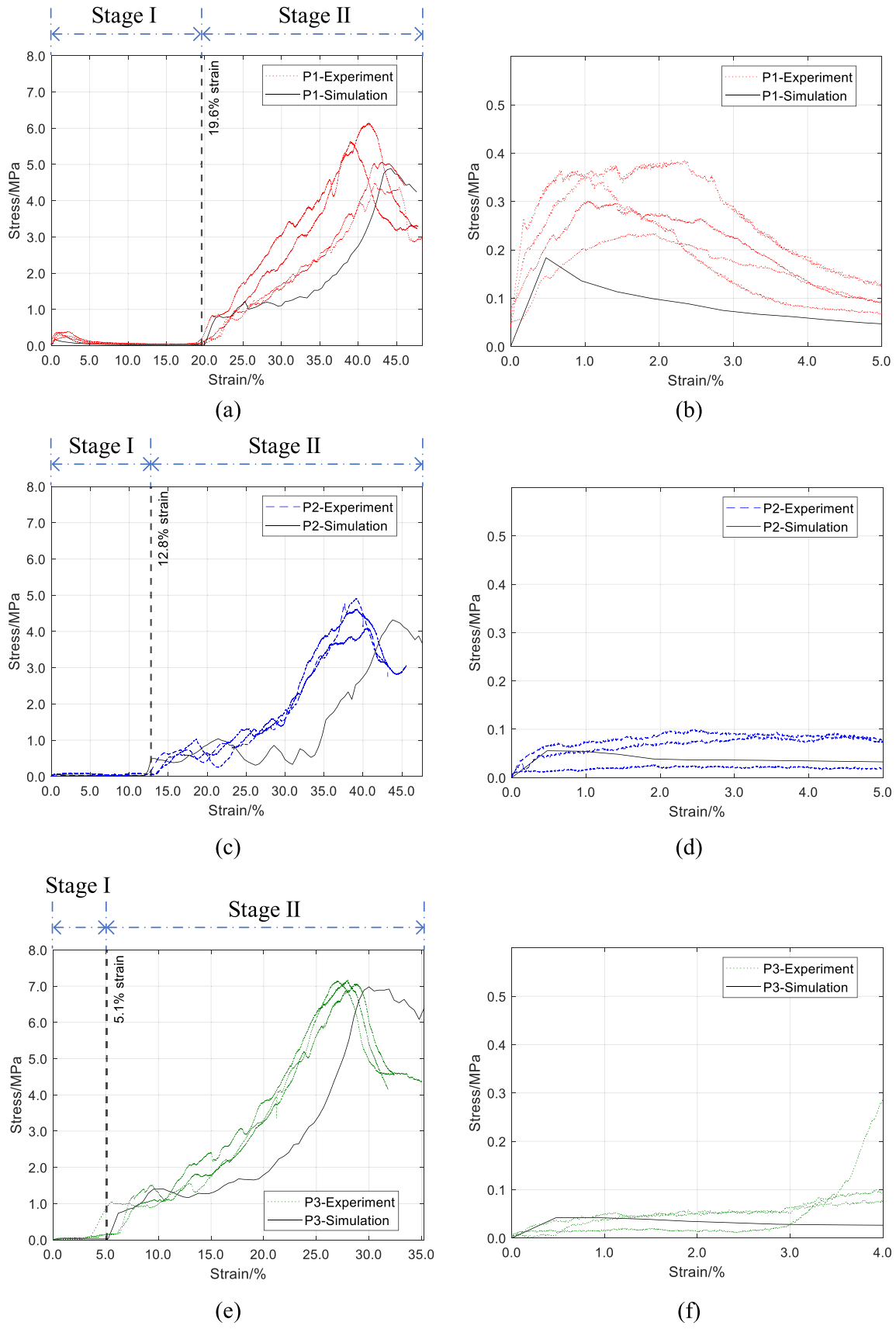

Fig. 10. Comparison of simulation and experimental results for stress-strain curves of ACCCs under uniaxial compression, (a) P1: 0–48% strain, (b) P1: 0–5% strain, (c) P2: 0–48% strain, (d) P2: 0–5% strain, (c) P3: 0–35% strain, (d) P3: 0–4% strain.

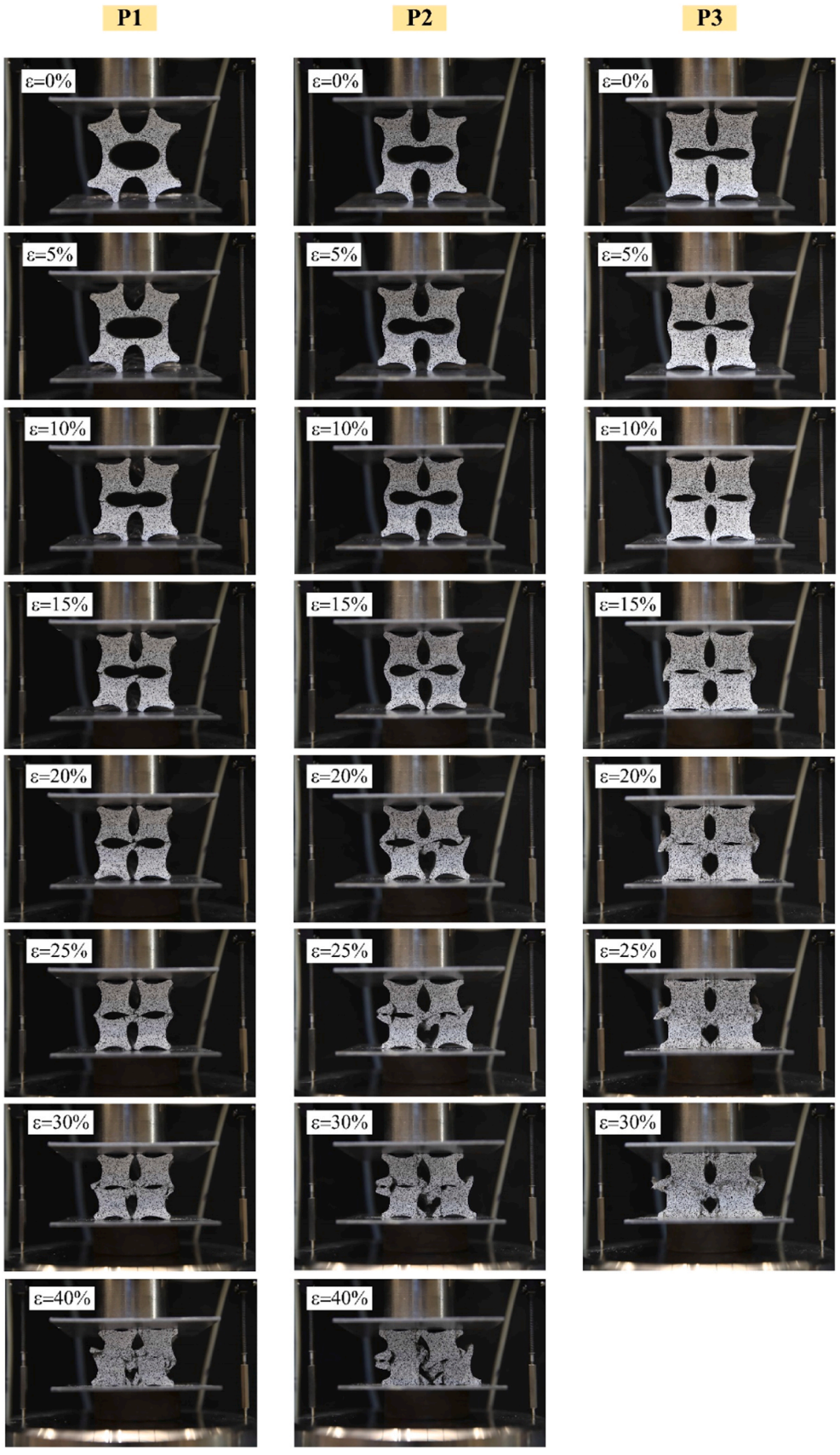

Fig. 11. The deformation process of ACCCs under compression.

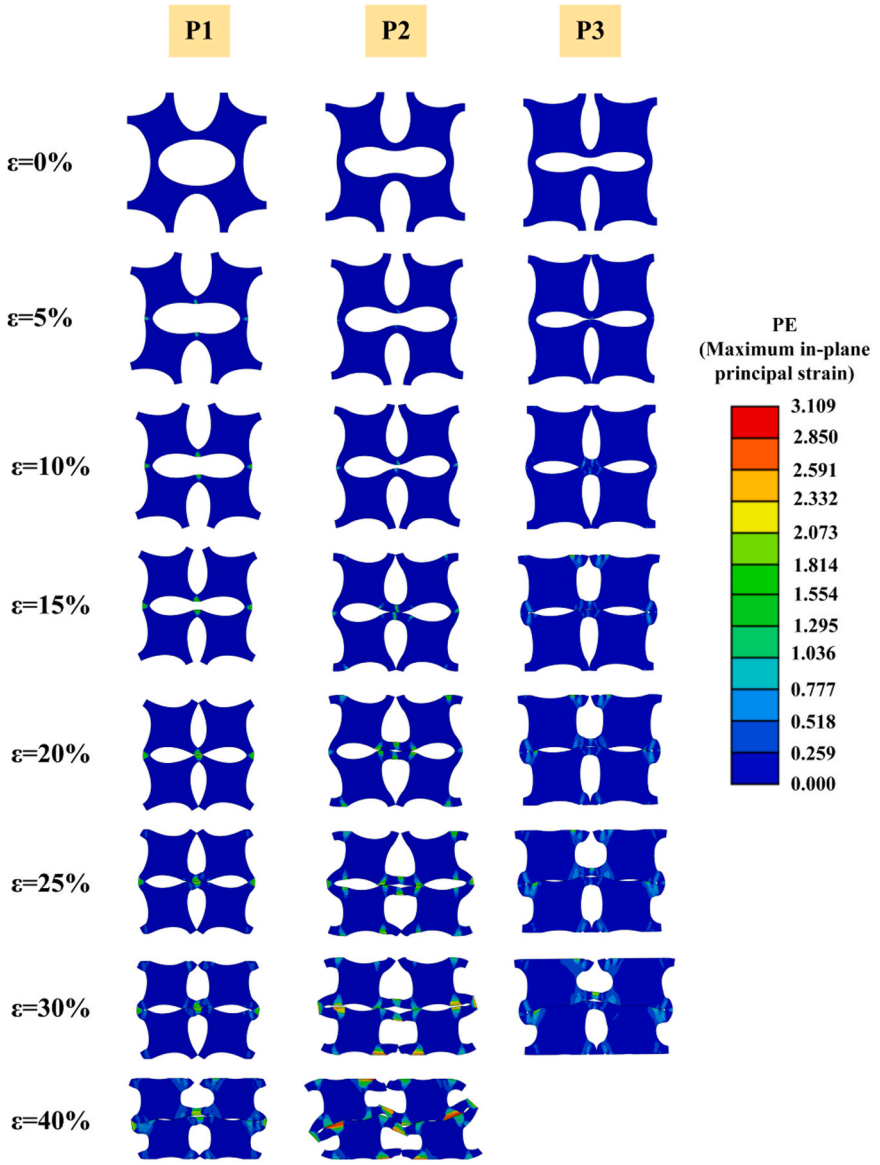

Fig. 12. The simulated deformation process of ACCCs under compression.

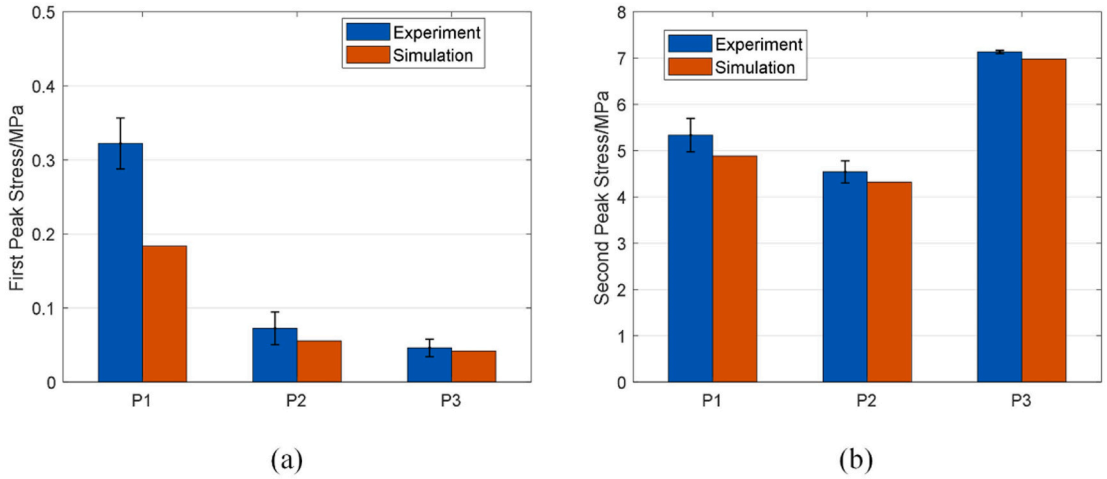

Fig. 13. Comparison of a) the first peak stress, (b) the second peak stress.

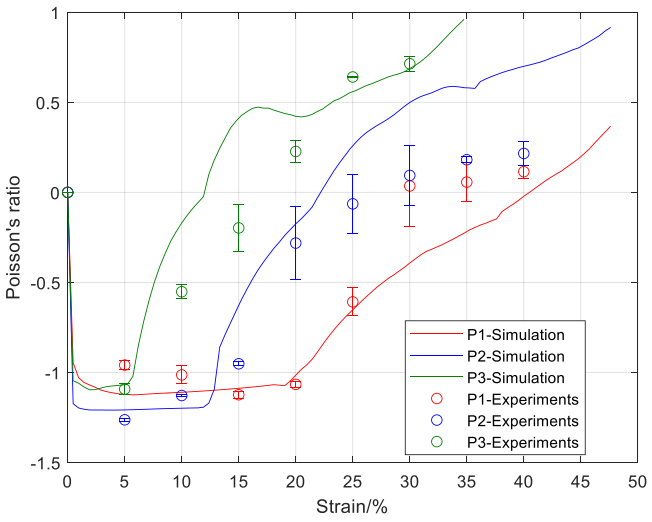

Fig. 14. Poisson's ratio variation for different shapes.

captures the variation in Poisson's ratio for ACCCs, exhibiting good agreement with the experimental measurements. As mentioned earlier, the edges of these elements with high plastic strain must adhere to the self-contact boundary conditions, unlike the crack without physical space. This discrepancy leads to the observed difference at high strains between the experiments and the models in Fig. 14.

5.1.3. Energy dissipation property

The energy dissipation of the ACCCs was calculated by integrating the stress-strain curve up to the current stress for each specimen in both the experiments and models in Fig. 15. Fig. 16a and b compare the energy dissipation and specific energy absorption (SEA) of ACCCs until the second peak stress, incorporating both experimental and numerical results. The experimental and simulated results in Fig. 15 and Fig. 16 exhibit good consistency. It can be found that in Fig. 15 that specimen P3 displays a notably slower rate of dissipated energy growth within the initial strain range of 0% to nearly 6%, in contrast to specimens P1 and P2. Conversely, beyond nearly 6% strain, specimen P3 exhibits a considerably rapid increase in energy dissipation, as compared to both P1 and P2. Similarly, specimen P2 displays a relatively slower rate of dissipated energy growth within the strain range of 0% to approximately 13%, when compared to P1. However, beyond approximately 13% strain, specimen P2 exhibits a relatively rapid increase in energy dissipation compared to specimen P1. As mentioned earlier, the discrepancy between experiments and models in Fig. 15 arises from the requirement for elements in the model with high plastic strain to adhere to self-contact boundary conditions, unlike a crack without physical space.

In Fig. 16a, Specimen P3 exhibits a higher energy dissipation until the second peak stress compared to specimens P1 and P2. This is because Specimen P3 presents high stress, which contributes to a 28.6% higher dissipation energy when compared to specimen P1. Specimen P2 demonstrates a lower energy dissipation, being only 11.6% less until the second peak stress, despite its reduced ductility resulting from a smaller compression space compared to Specimen P1. The alleviation of stress concentration allows the peanut shaped ACCCs to dissipate a substantial amount of energy, thereby showcasing their enhanced toughness. In Fig. 16b, there was also a comparison of specific energy absorption considering volume. Specimen P2 exhibits a 21.9% lower specific energy absorption compared to Specimen P1, while Specimen P3 shows a 14.8% lower specific energy absorption compared to Specimen P1. This is attributed to the lower volume of Specimen P1 chosen in this study (see Table 1), resulting in higher specific energy absorption.

The energy absorption efficiency E_a (ranging from zero to unity) can be calculated as [30,31]:

$$E_a = \frac{\int_0^{\varepsilon_m} \sigma d\varepsilon}{\sigma_m} \tag{16}$$

where ε_m is the current strain. σ_m is the current stress.

In Fig. 17, the energy absorption efficiency of ACCCs is still divided into two stages, determined by the cut-off strain associated with the self-contact of the central hole. The cut-off strains are approximately 21%, 13%, and 6% for specimens P1, P2, and P3, respectively. In Stage I, specimen P1 exhibits superior energy absorption efficiency compared to both specimens P2 and P3, while specimen P2 demonstrates greater efficiency than specimen P3. Conversely, during Stage II, specimen P1 displays diminished energy absorption efficiency relative to both specimens P2 and P3. Furthermore, specimen P3 manifests a slightly higher energy absorption efficiency than specimen P2. Hence, when compared to elliptical-shaped ACCCs, peanut shaped ACCCs exhibit reduced energy absorption efficiency in Stage I but demonstrate increased efficiency in Stage II. Fig. 17 additionally depicts the model-calculated energy absorption efficiency, demonstrating close agreement with experimental measurements. However, as previously stated, the observed discrepancy at high strains between experiments and models is also attributed to the requirement for elements in the model with substantial plastic strain to adhere to self-contact boundary conditions, in contrast to a crack without physical space in experiments.

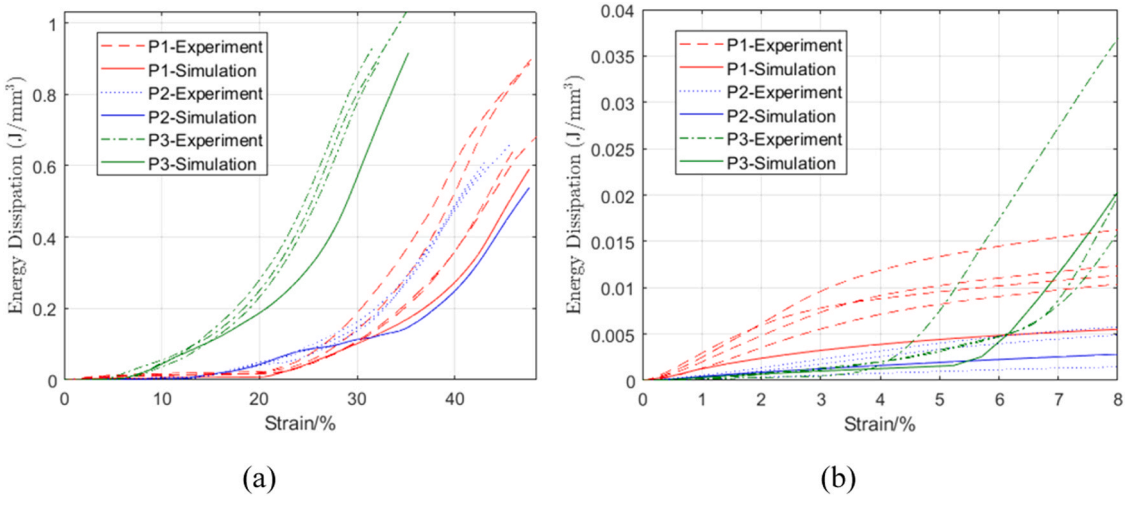

Fig. 15. Comparison of a) the energy dissipation within the strain range of 0–48%, b) the energy dissipation within the strain range of 0–8%.

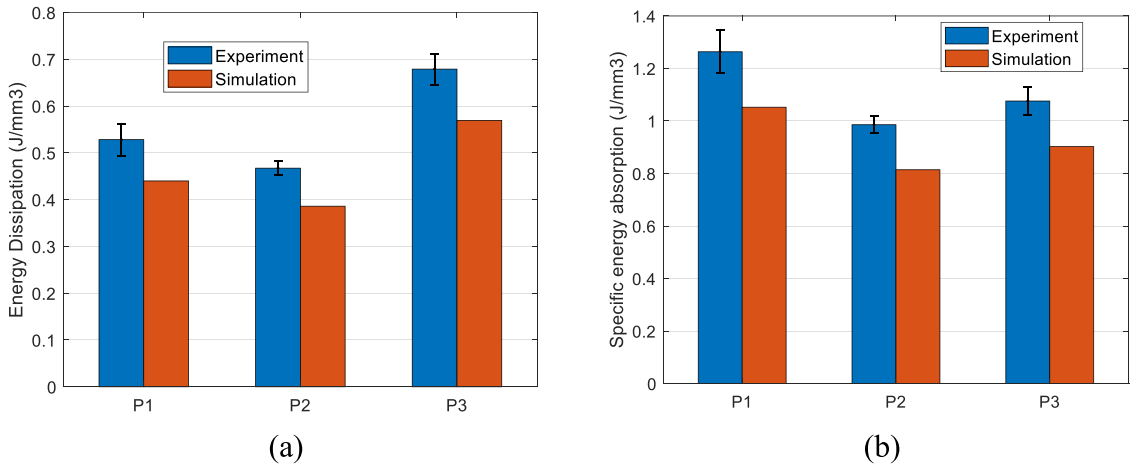

Fig. 16. Comparison of the energy dissipation until the second peak stress, (a) energy dissipation by integrating the stress-strain curve, (b) specific energy absorption.

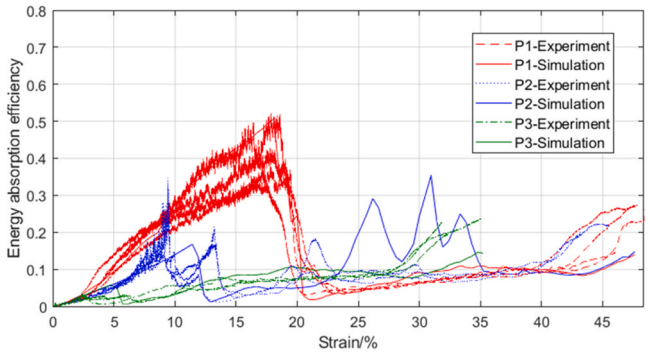

Fig. 17. Energy absorption efficiency of different ACCCs.

5.1.4. Strain distribution analysed by DIC

The strain distribution of ACCCs is show in Fig. 18 based on DIC results over an initial compressive strain range from 0% to 5%. Notably, it is discernible that the P1 specimen exhibits a higher localized strain compared to the P2 and P3 specimens. This indicates that the elliptical specimen experiences more extensive damage during the compression process than the peanut shaped specimens.

5.2. Cyclic test results

5.2.1. Cyclic behavior of ACCCs

Fig. 19 shows the mechanical response of ACCCs under cyclic loading, spanning 10 cycles. It is found that all ACCC specimens exhibit a sinusoidal stress response corresponding to the sinusoidal displacement loading.

Most notably, the ACCCs exhibit remarkable structural deformation recovery upon the release of compressive loading during cyclic tests. The ACCC specimens strive to return to their original shape, albeit with some plastic deformation or damage. This behavior is uncommon in traditional cementitious structures. The term “compressive deformation resilience“ or “recoverable deformation elasticity” is used to characterize the structural recovery or elastic behavior of the entire structure upon the release of compressive stress. Further details can be found in the videos included in the Supplementary data. In each loading cycle, the stress rises concomitantly with the increase in the compressive displacement. Upon reaching the maximum displacement, the ACCC specimen reaches its peak stress, with stress directly correlating to the applied displacement. Subsequently, as the loading plate gradually moves away from the ACCCs, the stress gradually diminishes to a nearly negligible level. The peak-to-peak stress for each specimen was calculated by averaging the values obtained over ten cycles in Fig. 19. Notably, Specimen P1 displays the lowest peak-to-peak stress at 0.0124 MPa, while P2 records 0.0314 MPa, and P3 exhibits the highest peak-to-peak stress of 0.6770 MPa among the three specimens. The elastic moduli of compressive resilience for specimens P1, P2, and P3 were calculated as 0.4 MPa, 0.99 MPa, and 21.33 MPa, respectively. Notably, the peanut shaped ACCCs exhibit superior recoverable deformation elasticity under cyclic loading compared to the elliptical-shaped ACCCs. Fig. 20 displays deformation resilience pattern of three ACCCs in each cycle of compression and subsequent release. Herein, each red point in one row represents the loading state within each sinusoidal cycle for three ACCCs. As illustrated in Appendix C, microscopic examination of three ACCC shapes after cyclic loading reveals distinct features. Elliptical-shaped ACCCs exhibit a predominant wide crack in their ligaments, accompanied by fiber twisting and fracturing at the fiber ends. In contrast, peanut shaped ACCCs tend to develop multiple thinner cracks in their ligaments, characterized by straight and smooth fiber ends, indicating a stronger fiber-bridging capacity.

Supplementary material related to this article can be found online at doi:10.1016/j.conbuildmat.2024.135539.

6. Conclusions

In this research, a novel type of peanut shaped ACCC exhibiting remarkable auxetic properties was designed and fabricated. Experiments and numerical modelling have been carried out to examine their compressive behavior, including peak strength, Poisson’s ratio variation, and energy dissipation capacity. In addition, cyclic tests were carried out to explore their compressive resilience properties. The following conclusions have been derived:

1. The auxetic behavior of peanut shaped ACCCs is a consequence of the rotation of sections facilitated by fiber bridging at the ligament of adjacent holes within the cementitious unit cell. In comparison to elliptical-shaped ACCCs, peanut shaped ACCCs can demonstrate a slightly more negative Poisson’s ratio, alleviate stress concentration, and enhance structural ductility. Peanut shaped ACCCs with a larger pseudo minor axis exhibit a more significant negative Poisson’s ratio and a longer duration of a negative Poisson’s ratio.
2. Peanut shaped ACCCs exhibit a compressive behavior characterized by two distinct stages, each featuring a peak stress. The onset of their second stage (Stage II) corresponds to the contact between the top and bottom ends of the peanut shaped hole. However, the initial peak stress in the first stage (Stage I) is lower for peanut shaped ACCCs when compared to elliptical-shaped ACCCs. In Stage II, peanut shaped ACCCs with a smaller pseudo minor axis demonstrate a higher

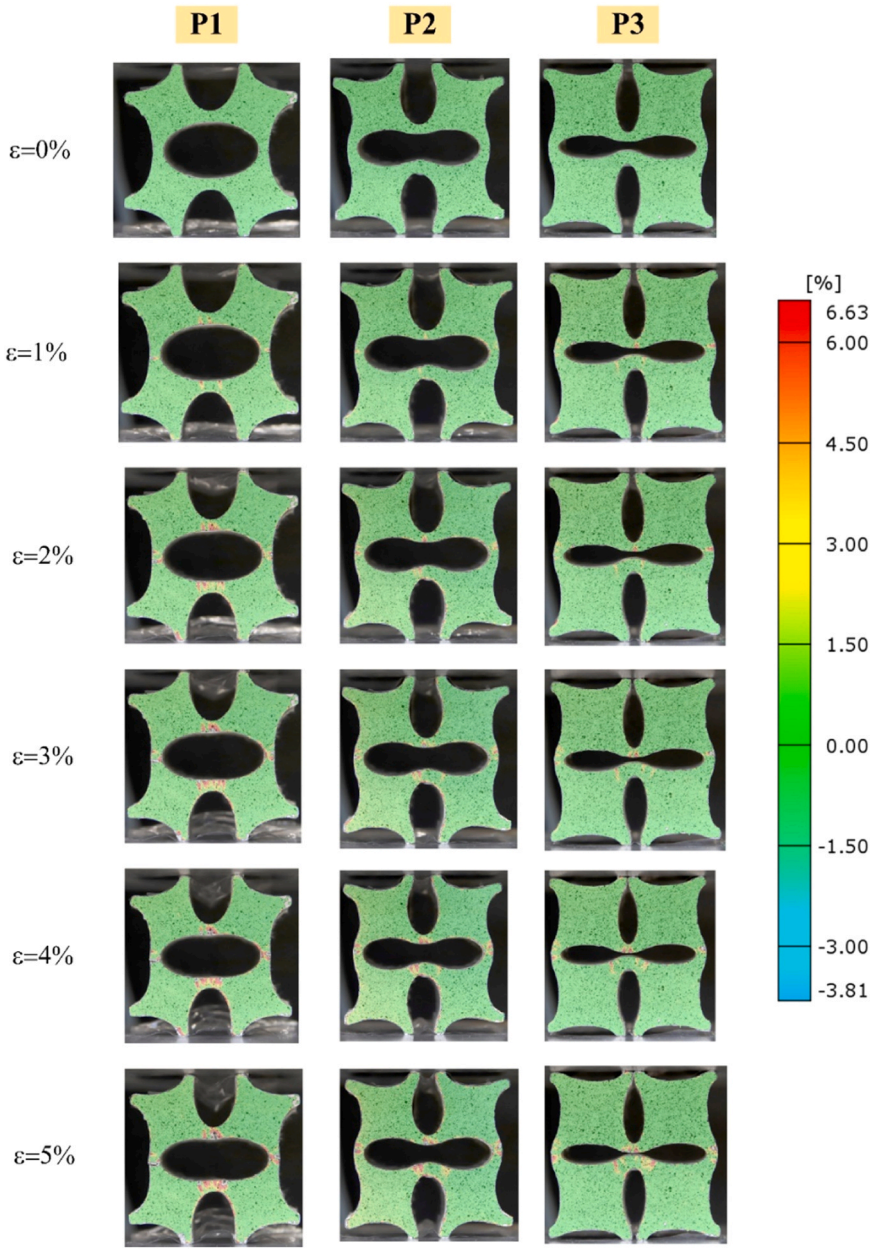

Fig. 18. Strain distribution obtained from DIC results.

second peak stress compared to those with a larger pseudo minor axis. The reduction of stress concentration enables peanut shaped ACCCs to dissipate substantial energy, showcasing enhanced toughness. In comparison to elliptical-shaped ACCCs, peanut shaped ACCCs exhibit lower energy absorption efficiency in Stage I but higher efficiency in Stage II.

3. The Concrete Damage Plasticity (CDP) Model is an effective tool for simulating the uniaxial compressive behavior of both elliptical-shaped and peanut shaped ACCCs. It accurately reproduces their deformation pattern, Poisson's ratio, stress-strain response, and energy dissipation characteristics.
4. Under cyclic loading following pre-compression, the peanut shaped ACCCs exhibit superior recoverable deformation elasticity, in comparison to their elliptical-shaped counterparts. The reason revealed by microscopic analysis is that elliptical-shaped ACCCs present one predominant wide crack in their ligaments, accompanied by fiber twisting and fracturing at the fiber ends. However, peanut shaped ACCCs tend to develop multiple thinner cracks in their ligaments, which are characterized by straight and smooth fiber ends, thus demonstrating a stronger fiber-bridging capacity.

The exceptional mechanical properties exhibited by peanut shaped ACCCs can be harnessed for the absorption of kinetic or impact energy within the realm of infrastructure. These potential applications areas include shock-absorbent bike lane pavements [4], speed hump in keeping vehicle speeds down, diagnostic seismic isolator, high toughness structure [32], engineered materials arresting systems (EMAS) [33] for mitigating the consequences of aircraft landing overruns. Moreover, the application of peanut shaped ACCCs opens up the potential for developing multi-functional cementitious materials in smart infrastructure, such as strain energy transformation-based energy harvesters [19,34–36], flexible sensor with self-sensing capabilities in structural health monitoring (SHM) [37–39], self-charging roads for electric vehicles [40].

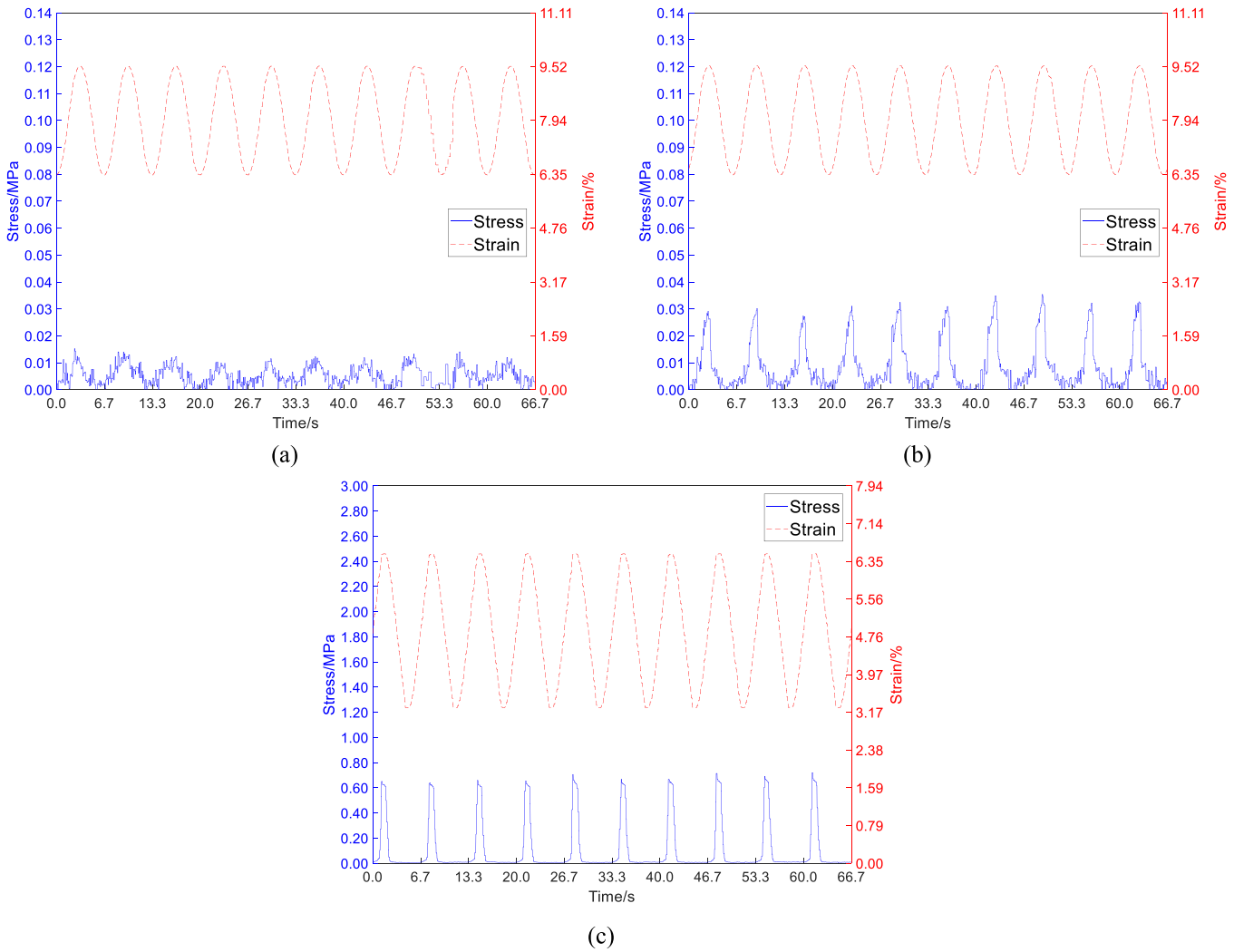

Fig. 19. Cyclic behavior of ACCCs specimens, (a) P1, (b) P2, (c) P3.

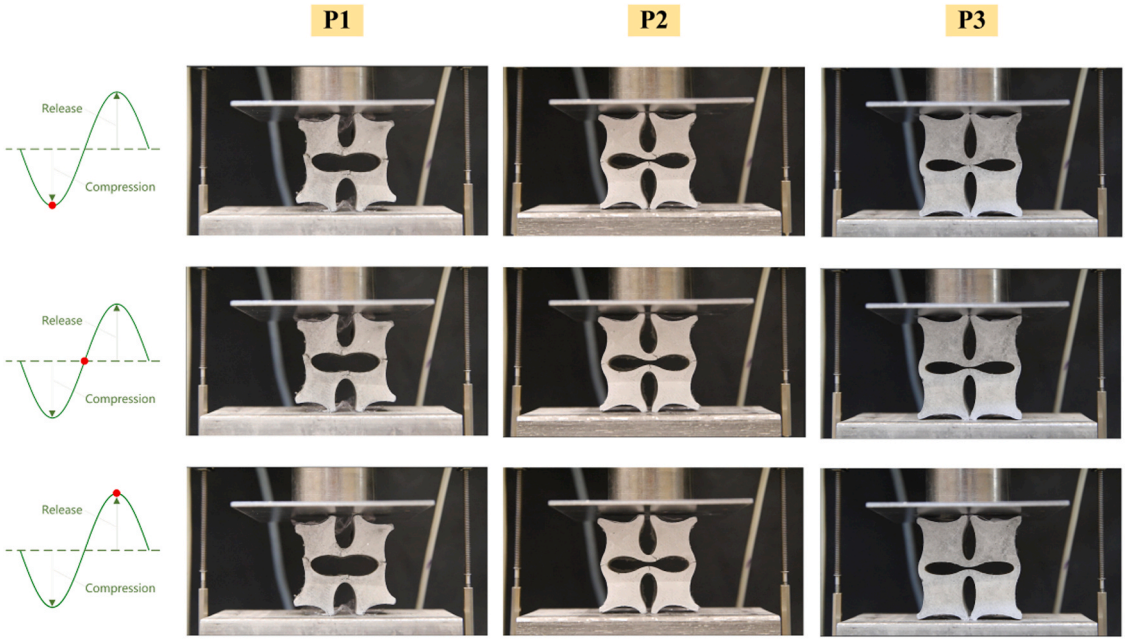

Fig. 20. Deformation resilience pattern of ACCCs under cyclic loading.

CRediT authorship contribution statement

Jinbao Xie: Writing – review & editing, Writing – original draft, Validation, Software, Methodology, Formal analysis, Data curation, Conceptualization. **Yading Xu**: Writing – review & editing, Methodology, Formal analysis, Conceptualization. **Zhaozheng Meng**: Writing – review & editing, Validation. **Minfei Liang**: Writing – review & editing, Visualization. **Zhi Wan**: Writing – review & editing, Visualization. **Branko Šavija**: Writing – review & editing, Validation, Supervision, Resources, Methodology, Funding acquisition, Conceptualization.

Declaration of Competing Interest

The authors declare that they have no known competing financial interests or personal relationships that could have appeared to influence the work reported in this paper.

Data availability

Data will be made available on request.

Acknowledgements

Jinbao Xie, Minfei Liang, and Zhi Wan would like to acknowledge the funding supported by China Scholarship Council (CSC) under the grant CSC No. 202006260045, 202007000027, 201906220205. The experimental part of the study was funded by the Dutch Research Council (NWO) through the Open Mind Project "Auxetic Concrete Energy Harvester", grant number 18764. Yading Xu, Zhaozheng Meng, Branko Šavija acknowledge the financial support of the European Research Council (ERC) within the framework of the ERC Starting Grant Project "Auxetic Cementitious Composites by 3D printing (ACC-3D)", Grant Agreement Number 101041342. Views and opinions expressed are however those of the author(s) only and do not necessarily reflect those of the European Union or the European Research Council. Neither the European Union nor the granting authority can be held responsible for them.

Appendix A

Comparison of compression behaviors between the unit cell and multiple cells in ACCCs.

In general, auxetic materials consist of repetitive unit cells. In our previous study [14], the compression behavior of ACCCs with elliptical-shaped multiple cells has been investigated by experiments and numerical models. Fig. A1 gives a compression behavior comparison between ACCCs with elliptical-shaped multiple cells and a single elliptical-shaped unit cell, based on the CDP model parameters in literature [14]. In the study [14], the elliptical-shaped unit cell in ACCCs is characterized by a sample length of 20 mm, a major axis of 10 mm, and a minor axis of 6 mm, as illustrated in Fig. A1a. Sixteen cells make up the elliptical-shaped multiple cells in ACCCs, as depicted in Fig. A1b. As depicted in Fig. A1b, the simulated stress-strain curve of the elliptical-shaped unit cell exhibits a good agreement with those of the elliptical-shaped multiple cells up to the second peak stress of the elliptical-shaped multiple cells, which occurs at nearly 25% strain. Beyond that point, the stress of the elliptical-shaped unit cell continues to increase until reaching its second peak stress at nearly 45% strain. However, the stress of the elliptical-shaped multiple cells starts to decrease after reaching its second peak stress at nearly 25% strain. This decline is attributed to the increased local asymmetric plastic strain in each elliptical-shaped unit cell, leading to additional asymmetric deformation of the entire structure through ligament transfer.

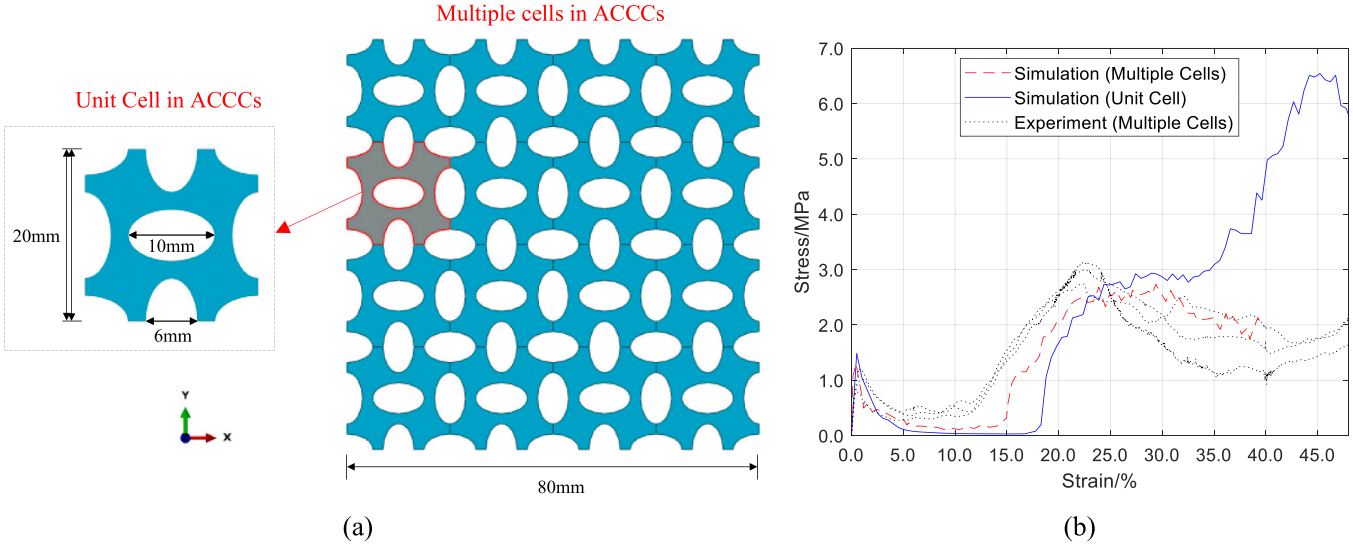

Fig. A1. Comparison of compression behaviors between the unit cell and multiple cells of the elliptical-shaped ACCC.

As shown in Fig. A2 in **Appendix A**, a comparison was also conducted between the unit cell and multiple cells of the peanut-shaped ACCC, based on the CDP model parameters in this study. The dimensions of the peanut-shaped unit cell are the same as P2 in this study. Sixteen peanut-shaped cells of the aforementioned size constitute the multiple cells in peanut-shaped ACCCs, as depicted in Fig. A2a. Similar to the elliptical-shaped ACCC, the simulated stress-strain curve of the peanut-shaped unit cell aligns well with that of the peanut-shaped multiple cells up to the second peak stress, occurring at nearly 20% strain (Fig. A2b). Beyond this point, the stress of the peanut-shaped unit cell continues to rise, reaching its second peak stress at nearly 40% strain, while the stress of the peanut-shaped multiple cells starts to decline after reaching their second peak stress at nearly 20% strain. This decline is due to local asymmetric plastic strain in each peanut-shaped unit cell, causing additional asymmetric deformation of the entire structure through ligament transfer. In future studies, additional experiments are needed for the multiple cells of the peanut-shaped ACCC to examine the

relationship between the unit cell and multiple cells of the peanut-shaped ACCC.

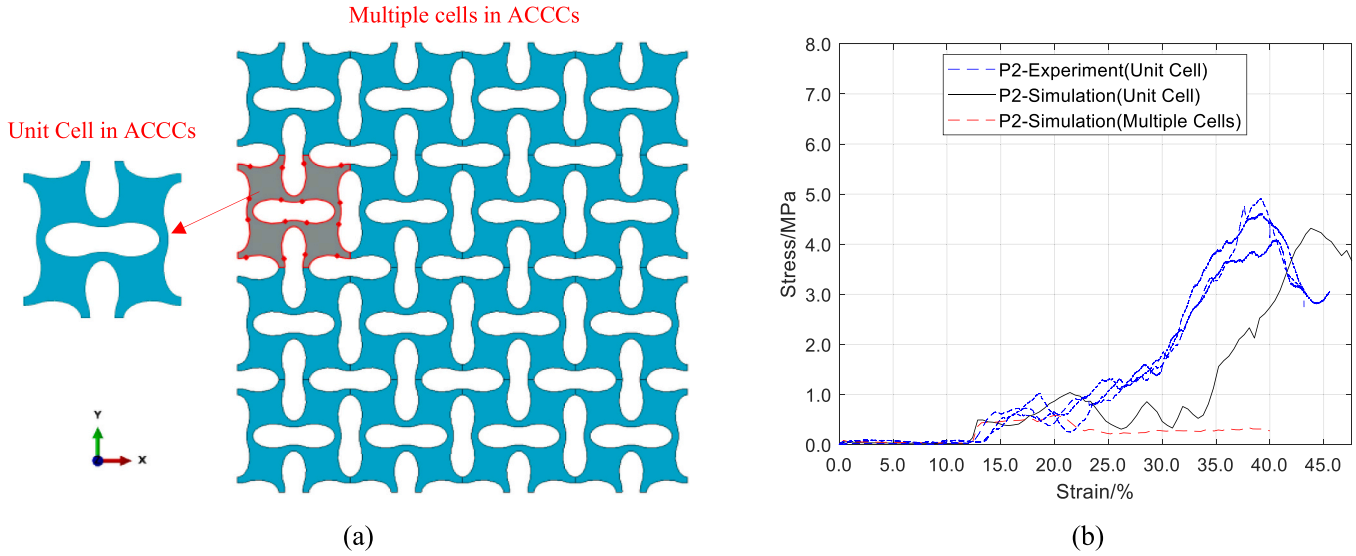

(a) (b)

Fig. A2. Comparison of compression behaviors between the unit cell and multiple cells of the peanut-shaped ACCC.

Appendix B

Additional details regarding the calculation of Eqs. (1)-(9) was provided in **Appendix B**.

As show in Fig. B1, the central point of the peanut-shaped hole is denoted by O in the Cartesian coordinate system. The center of the right ellipse is identified as E' with an x-coordinate of $a+c$. Its elliptical equation is

$$\frac{(x-(a+c))^2}{a^2}+\frac{y^2}{b^2}=1 \tag{B1}$$

Derived from Eq. (B1), the distance of line PQ (i.e., the x coordinate of point K) can be obtained as

$$l_{PQ}=a+c-\sqrt{a^2\left(1-\frac{d^2}{b^2}\right)} \tag{B2}$$

For the triangle marked by blue, the pythagorean theorem can be applied as

$$\left(a+c-\sqrt{a^2\left(1-d^2/b^2\right)}\right)^2+(R-e)^2=R^2 \tag{B3}$$

Then, the radius of R of the auxiliary circle can be obtained by

$$R=\frac{\left(a+c-\sqrt{a^2\left(1-d^2/b^2\right)}\right)^2+e^2}{2e} \tag{B4}$$

The central angle corresponding to the $PO'S$ sector can be calculated as

$$\theta=2*\arctan\left(\frac{l_{PQ}}{R-e}\right) \tag{B5}$$

In Fig. B1, the area where one auxiliary circles and the green rectangle intersect can be obtained by subtracting the triangle formed by the points $PO'S$ from the sector formed by the same three points.

$$A_{1a}=A_1/2.0=\frac{1}{2}\theta R^2-l_{PQ}*\left(R-e\right) \tag{B6}$$

In Fig. B1, the area where one peanut-shaped hole and the green rectangle intersect is as follows:

$$A_{2a}=A_2/2.0=2\int_c^{a+c-\sqrt{a^2\left(1-d^2/b^2\right)}}\sqrt{b^2\left(1-\frac{(x-(a+c))^2}{a^2}\right)}dx \tag{B7}$$

The aforementioned integral can be solved using the substitution method with trigonometric functions. Thus,

$$A_{2a}=A_2/2.0=0.5ab*\sin\left(2\left(\arccos\left(-\sqrt{1-d^2/b^2}\right)-\pi\right)\right)-ab*\left(\arccos\left(-\sqrt{1-d^2/b^2}\right)-\pi\right) \tag{B8}$$

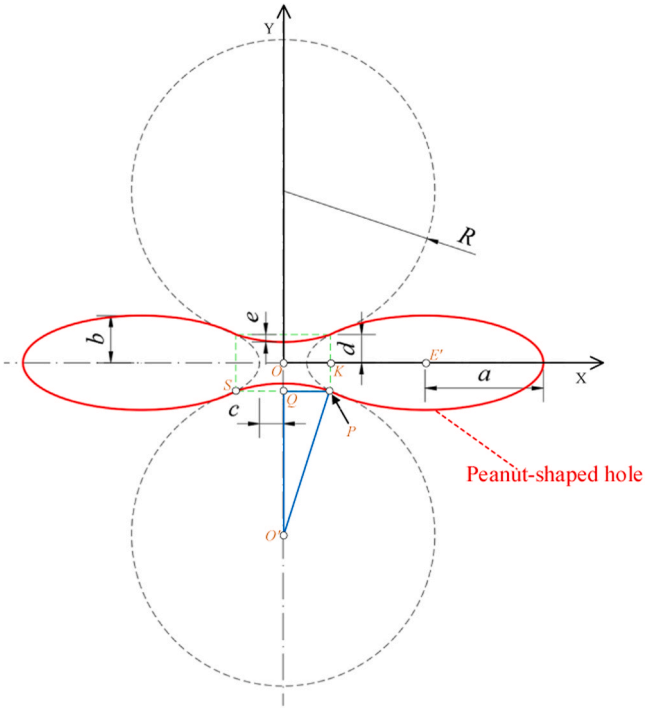

Fig. B1. Elaboration on the calculations for geometric parameters of the Peanut-shaped hole.

Appendix C

Microstructural analysis of fiber bridging behaviors for ACCCs.

As shown in Fig. C1, a digital optical microscope was used to analyze the fiber bridging and pull-out behaviors at the crack locations of ligament between neighboring holes in three ACCCs specimens after cyclic loading. As shown in Fig. C1, a singular primary crack with a substantial width was observed in the ligament of specimen P1. A significant occurrence of fiber pull-outs was observed, often accompanied by fiber twisting and fracturing at the fiber ends. Consequently, P1 specimen, i.e., elliptical ACCCs, exhibited the weakest bridging capability and displayed relatively poor recoverable deformation elasticity. In the case of P2 specimen, multiple cracks in its ligament locations were observed, with a reduction in crack width. Nevertheless, a primary crack remained discernible. Compared to P1, the extent of fiber pull-out was mitigated, and the pulled fibers exhibited straight configuration with smooth ends. As a result, P2 specimen demonstrated a stronger fiber bridging capability and thus a notable degree of recoverable deformation elasticity. For P3 specimen, an increase in the number of cracks was observed at the ligament, while their widths were significantly reduced. Fiber pull-out was rarely observed, with the majority of fibers remaining bridged at both ends within the cement matrix. Hence, P3 specimen continued to demonstrate sufficient fiber bridging capacity, leading to the highest level of recoverable deformation elasticity.

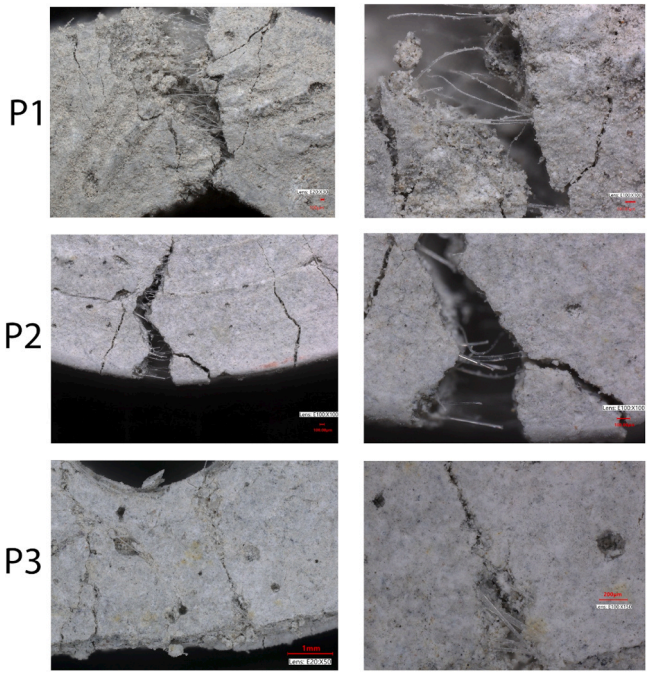

Fig. C1. Microstructural analysis of fiber bridging behaviors for ACCCs

.

References

[1] B. Peng, Y. Wei, Y. Qin, J. Dai, Y. Li, A. Liu, Y. Tian, L. Han, Y. Zheng, P. Wen, Machine learning-enabled constrained multi-objective design of architected materials, Nat. Commun. 14 (2023) 6630, https://doi.org/10.1038/s41467-023-42415-y.

[2] M. Moini, J. Olek, J.P. Youngblood, B. Magee, P.D. Zavattieri, Additive manufacturing and performance of architectured cement-based materials, Adv. Mater. 30 (2018) 1802123, https://doi.org/10.1002/adma.201802123.

[3] S.M. Sajadi, C.S. Tiwary, A.H. Rahmati, S.L. Eichmann, C.J. Thaemlitz, D. Salpekar, A.B. Puthirath, P.J. Boul, M.M. Rahman, A. Meiyazhagan, P.M. Ajayan, Deformation resilient cement structures using 3D-printed molds, iScience 24 (2021) 102174, https://doi.org/10.1016/j.isci.2021.102174.

[4] K. Barri, Q. Zhang, J. Kline, W. Lu, J. Luo, Z. Sun, B.E. Taylor, S.G. Sachs, L. Khazanovich, Z.L. Wang, A.H. Alavi, Multifunctional nanogenerator-integrated metamaterial concrete systems for smart civil infrastructure, Adv. Mater. 35 (2023) 2211027, https://doi.org/10.1002/adma.202211027.

[5] Z. Wan, Y. Xu, S. He, Y. Chen, J. Xie, B. Šavija, Direct ink writing of vascularized self-healing cementitious composites, Cem. Concr. Compos. 144 (2023) 105295, https://doi.org/10.1016/j.cemconcomp.2023.105295.

[6] W. Zhou, Y. Zhang, L. Ma, V.C. Li, Influence of printing parameters on 3D printing engineered cementitious composites (3DP-ECC), Cem. Concr. Compos. 130 (2022) 104562, https://doi.org/10.1016/j.cemconcomp.2022.104562.

[7] V.C. Li, On engineered cementitious composites (ECC) a review of the material and its applications, J. Adv. Concr. Technol. 1 (2003) 215–230, https://doi.org/10.3151/jact.1.215.

[8] V.C. Li, Tailoring ECC for special attributes: a review, Int. J. Concr. Struct. Mater. 6 (2012) 135–144, https://doi.org/10.1007/s40069-012-0018-8.

[9] E.-H. Yang, V.C. Li, Tailoring engineered cementitious composites for impact resistance, Cem. Concr. Res. 42 (2012) 1066–1071, https://doi.org/10.1016/j.cemconres.2012.04.006.

[10] K. Tosun-Felekoğlu, B. Felekoğlu, R. Ranade, B.Y. Lee, V.C. Li, The role of flaw size and fiber distribution on tensile ductility of PVA-ECC, Compos. Part B: Eng. 56 (2014) 536–545, https://doi.org/10.1016/j.compositesb.2013.08.089.

[11] C.-C. Hung, Y.-F. Su, K.-H. Yu, Modeling the shear hysteretic response for high performance fiber reinforced cementitious composites, Constr. Build. Mater. 41 (2013) 37–48, https://doi.org/10.1016/j.conbuildmat.2012.12.010.

[12] M. Ohno, M. Pierre, K. Imagawa, T. Ishida, Simulation and learning-driven design for architected cement-based materials, J. Build. Eng. 65 (2023) 105768, https://doi.org/10.1016/j.jobe.2022.105768.

[13] W. Zhou, W. McGee, H.S. Gökçe, V.C. Li, A bio-inspired solution to alleviate anisotropy of 3D printed engineered cementitious composites (3DP-ECC): Knitting/tilting filaments, Autom. Constr. 155 (2023) 105051, https://doi.org/10.1016/j.autcon.2023.105051.

[14] Y. Xu, E. Schlangen, M. Luković, B. Šavija, Tunable mechanical behavior of auxetic cementitious cellular composites (CCCs): Experiments and simulations, Constr. Build. Mater. 266 (2021) 121388, https://doi.org/10.1016/j.conbuildmat.2020.121388.

[15] X. Ren, R. Das, P. Tran, T.D. Ngo, Y.M. Xie, Auxetic metamaterials and structures: a review, Smart Mater. Struct. 27 (2018) 023001, https://doi.org/10.1088/1361-665X/aaa61c.

[16] K.E. Evans, Auxetic polymers: a new range of materials, Endeavour 15 (1991) 170–174, https://doi.org/10.1016/0160-9327(91)90123-S.

[17] W. Jiang, X. Ren, S.L. Wang, X.G. Zhang, X.Y. Zhang, C. Luo, Y.M. Xie, F. Scarpa, A. Alderson, K.E. Evans, Manufacturing, characteristics and applications of auxetic foams: a state-of-the-art review, Compos. Part B: Eng. 235 (2022) 109733, https://doi.org/10.1016/j.compositesb.2022.109733.

[18] Y. Xu, H. Zhang, E. Schlangen, M. Luković, B. Šavija, Cementitious cellular composites with auxetic behavior, Cem. Concr. Compos. 111 (2020) 103624, https://doi.org/10.1016/j.cemconcomp.2020.103624.

[19] J. Xie, Y. Xu, Z. Wan, A. Ghaderiaram, E. Schlangen, B. Šavija, Auxetic cementitious cellular composite (ACCC) PVDF-based energy harvester, Energy Build. 298 (2023) 113582, https://doi.org/10.1016/j.enbuild.2023.113582.

[20] H. Wang, Y. Zhang, W. Lin, Q.-H. Qin, A novel two-dimensional mechanical metamaterial with negative Poisson's ratio, Comput. Mater. Sci. 171 (2020) 109232, https://doi.org/10.1016/j.commatsci.2019.109232.

[21] Y. Zhu, J. Wang, X. Cai, Z. Xu, Y. Wen, Cyclic behavior of ellipse and peanut-shaped perforated buckling-restrained braces, Eng. Struct. 291 (2023) 116432, https://doi.org/10.1016/j.engstruct.2023.116432.

[22] B. Taherkhani, M. Bodaghi, S.S. Mousavi Nejad Souq, M. Malmir Chegini, M. Nemati, Novel Linear Piezo-resistive auxetic meta-sensors with low Young's modulus by a core–shell conceptual design and electromechanical modelling, Macromol. Mater. Eng. 308 (2023) 2300219, https://doi.org/10.1002/mame.202300219.

[23] J. Xie, R. Zhang, T. Liu, C. Zhou, T. Gu, B. Chen, Y. Chen, L.-J. Jia, Growth of random polyhedral void in structural steel based on micromechanical RVE simulations, Adv. Eng. Softw. 175 (2023) 103344, https://doi.org/10.1016/j.advengsoft.2022.103344.

[24] J. Xie, R. Zhang, T. Liu, C. Zhou, L.-J. Jia, Effect of initial void shape on void growth of structural steels based on micromechanical RVE models, J. Mater. Civ. Eng. 34 (2022) 04022010, https://doi.org/10.1061/(ASCE)MT.1943-5533.0004150.

[25] L. Wu, M. Mustafa, J. Segurado, L. Noels, Second-order computational homogenisation enhanced with non-uniform body forces for non-linear cellular materials and metamaterials, Comput. Methods Appl. Mech. Eng. 407 (2023) 115931, https://doi.org/10.1016/j.cma.2023.115931.

[26] Y. von Hoegen, S. Hellebrand, L. Scheunemann, J. Schröder, On the realization of periodic boundary conditions for hexagonal unit cells, Finite Elem. Anal. Des. 229 (2024) 104067, https://doi.org/10.1016/j.finel.2023.104067.

[27] A. Thalhamer, M. Fleisch, C. Schuecker, P.F. Fuchs, S. Schlögl, M. Berer, A black-box optimization strategy for customizable global elastic deformation behavior of unit cell-based tri-anti-chiral metamaterials, Adv. Eng. Softw. 186 (2023) 103553, https://doi.org/10.1016/j.advengsoft.2023.103553.
[28] Y. Zhou, L.J. Sluys, R. Esposito, An improved mean-field homogenization model for the three-dimensional elastic properties of masonry, Eur. J. Mech. - A/Solids 96 (2022) 104721, https://doi.org/10.1016/j.euromechsol.2022.104721.
[29] R.J.M. Bol, B. Šavija, Micromechanical models for FDM 3D-printed polymers: a review, Polymers 15 (2023) 4497, https://doi.org/10.3390/polym15234497.
[30] J. Miltz, G. Gruenbaum, Evaluation of cushioning properties of plastic foams from compressive measurements, Polym. Eng. Sci. 21 (1981) 1010–1014, https://doi.org/10.1002/pen.760211505.
[31] Y. Xu, B. Šavija, 3D auxetic cementitious-polymeric composite structure with compressive strain-hardening behavior, Eng. Struct. 294 (2023) 116734, https://doi.org/10.1016/j.engstruct.2023.116734.
[32] Y. Chen, Y. Zheng, Y. Zhou, W. Zhang, W. Li, W. She, J. Liu, C. Miao, Multi-layered cement-hydrogel composite with high toughness, low thermal conductivity, and self-healing capability, Nat. Commun. 14 (2023) 3438, https://doi.org/10.1038/s41467-023-39235-5.
[33] M. Ketabdari, E. Toraldo, M. Crispino, V. Lunkar, Evaluating the interaction between engineered materials and aircraft tyres as arresting systems in landing overrun events, Case Stud. Constr. Mater. 13 (2020) e00446, https://doi.org/10.1016/j.cscm.2020.e00446.
[34] Y.-F. Su, R.R. Kotian, N. Lu, Energy harvesting potential of bendable concrete using polymer based piezoelectric generator, Compos. Part B: Eng. 153 (2018) 124–129, https://doi.org/10.1016/j.compositesb.2018.07.018.
[35] Q. Gao, W. Li, Y. Shi, W.-H. Liao, G. Yin, J. Li, C. Wang, R. Qiu, A rotating auxetic energy harvester for vehicle wheels, Eng. Struct. 288 (2023) 116190, https://doi.org/10.1016/j.engstruct.2023.116190.
[36] J. Zhao, G. Karalis, M. Liebscher, L. Tzounis, T. Köberle, D. Fischer, F. Simon, M. A. Aiti, G. Cuniberti, V. Mechtcherine, Mineral-impregnated carbon-fiber based reinforcing grids as thermal energy harvesters: a proof-of-concept study towards multifunctional building materials, Energy Build. 298 (2023) 113564, https://doi.org/10.1016/j.enbuild.2023.113564.
[37] L.R. de Souza, M. Pimentel, G. Milone, J.C. Tristão, A. Al-Tabbaa, Carbon nanofibers grown in CaO for self-sensing in mortar, Materials 15 (2022) 4951, https://doi.org/10.3390/ma15144951.
[38] X. Wang, A. Al-Tabbaa, S.K. Haigh, Measurement techniques for self-sensing cementitious composites under flexure, Cem. Concr. Compos. 142 (2023) 105215, https://doi.org/10.1016/j.cemconcomp.2023.105215.
[39] X. Wang, B. Cao, C. Vlachakis, A. Al-Tabbaa, S.K. Haigh, Characterization and piezo-resistivity studies on graphite-enabled self-sensing cementitious composites with high stress and strain sensitivity, Cem. Concr. Compos. 142 (2023) 105187, https://doi.org/10.1016/j.cemconcomp.2023.105187.
[40] N. Chanut, D. Stefaniuk, J.C. Weaver, Y. Zhu, Y. Shao-Horn, A. Masic, F.-J. Ulm, Carbon–cement supercapacitors as a scalable bulk energy storage solution, Proc. Natl. Acad. Sci. 120 (2023) e2304318120, https://doi.org/10.1073/pnas.2304318120.